Biochemical and structural insights into the auto-inhibited state of Mical1 and its activation by Rab8

Amrita Rai[1,*], Petra Janning[2], Ingrid R. Vetter[3] and Roger S. Goody[1]

[1]Department of Structural Biochemistry, Max Planck Institute of Molecular Physiology, Otto-Hahn-Strasse 11, 44227 Dortmund, Germany

[2]Department of Chemical Biology, Max Planck Institute of Molecular Physiology, Otto-Hahn-Strasse 11, 44227 Dortmund, Germany

[3]Department of Mechanistic Cell Biology, Max Planck Institute of Molecular Physiology, Otto-Hahn-Strasse 11, 44227 Dortmund, Germany

[*]Corresponding author: Amrita Rai (amrita.rai@mpi-dortmund.mpg.de)

Abstract

Mical1 regulates F-actin dynamics through the reversible oxidation of actin, a process controlled by its interactions with various proteins. Upon binding to Rab8 family members, Mical1 links endosomes to the cytoskeleton, promoting F-actin disassembly. In the absence of Rab, Mical1 exists in an auto-inhibited state, but its biochemical characterization remains incomplete. Our study reveals that the N-terminal MO-CH-LIM domains of Mical1 form an intramolecular complex with its C-terminal bMERB domain. Mutational analysis, guided by the AlphaFold2 model, identifies critical residues at the binding interface. Additionally, we demonstrate that full-length Mical1 binds to Rab8 in a 1:2 stoichiometry, thereby releasing auto-inhibition. Through structure-based mutational studies, we uncover allostery between the N and C-terminal Rab binding sites. Notably, Rab binding at the high-affinity C-terminal site precedes binding at the N-terminal site, suggesting a sequential binding mode. These findings elucidate how Rab8 binding releases the MO-CH-LIM domains from the Mical1 bMERB domain, facilitating interactions with other proteins and the actin cytoskeleton, thereby modulating actin dynamics.

Keywords: Mical1; Rab8, Rab10; Rab effectors; auto-inhibition; F-actin; human; biochemistry; biophysics; structural biology

Introduction

Actin dynamics is a highly controlled process, and the precise assembly and disassembly of actin is necessary for many cellular processes, including motility, adhesion, morphogenesis, and cytokinesis[1-3]. Actin-binding proteins (ABPs) are known to control filament polymerization (F-actin), its organization (bundling), and actin disassembly (G-actin). Apart from ABPs, actin post-translational modifications such as phosphorylation, oxidation, acetylation, arginylation, SUMOylation, ubiquitination, and others, regulate actin dynamics, fine-tune actin organization, and its interaction with ABPs[4]. The Molecule Interacting with CasL (Mical) protein family members include Mical1, Mical2, and Mical3, which are monooxygenases that oxidize actin and regulate cytoskeleton organization in the presence of the coenzyme NADPH and of O_2[5]. Mical1 specifically oxidizes Met44 and Met47 of the DNaseI-binding loop (D-loop) in actin monomers[6]. These residues are involved in bridging actin subunits, thereby regulating F-actin stability[6]. Methionine oxidation leads to F-actin depolymerization, a process that can be selectively reversed by methionine sulfoxide reductases. For example, MsrB reduces Met44 and Met47 of oxidized monomeric actin (G-actin), leading to the repolymerization of actin[7,8]. Mical proteins play a crucial role in actin assembly regulation during muscle organization, axon guidance, drosophila bristle development, cell shape, cell viability, cardiovascular integrity, vesicular trafficking, and regulation of nuclear actin[9]. Mical1 has been implicated in several different cancers, including pancreatic[10], breast[11], gastric[12], colorectal[13], and melanoma[14] as well as in neurological and mental health disorders such as neurodegeneration[15], spinal cord injury[16], and epilepsy[17].

Mical family members contain an N-terminal monooxygenase (MO) domain which plays a crucial role in actin-depolymerization, a calponin homology (CH) domain, a LIM (Lin-11, Isl-1, and Mec-3) domain which provides a protein-protein interaction interface, and a C-terminal bMERB domain that interacts with Rab proteins[5,18]. Apart from these domains, Mical family members have a proline-rich region that interacts with SH3 domain-containing proteins[19]. Mical1 plays a crucial role in synapse development[20]. Mical1 and Mical3 are required for cytokinesis and vesicular trafficking. They regulate these processes by regulating F-actin dynamics by disassembling the actin filaments. Mical-like (MICAL-L) family members lack the MO domain and play critical roles in vesicular trafficking[21]. Humans have two Mical-like proteins (Mical-L1 and Mical-L2/JRAB) whereas Drosophila has a single Mical and a single Mical-like protein. Several studies have reported that in the absence of stimuli, the Micals and Mical-like family members exist in an auto-inhibited state[9]. However, biochemical, and structural characterization of the auto-inhibited state is missing.

Rab GTPases are players that have a crucial role in vesicular trafficking and more than 60 Rabs have been reported for humans[22]. Similar to other small GTPases, they act as molecular switches, switching

between GTP-bound active state and GDP-bound inactive state[22]. The switching process is spatiotemporally regulated by guanine nucleotide exchange factors (GEFs) which facilitate the nucleotide exchange from GDP to GTP and their GTPase activity is enhanced by GTPase-activating proteins (GAPs)[23-25]. In the active GTP bound state, Rabs interacts with specific effector molecules to execute distinct downstream functions[22]. MICAL family members are one such Rab8 family effector. It has been shown that the binding of Rab molecules activates these family members by releasing auto-inhibition[26,27]. We have previously shown that in the case of some family members, such as Mical1/3 and EHBP1L1, Rab binds to the bMERB domain in a 1:2 stoichiometry, whereas other bMERB family members have only a C-terminal high affinity binding site[28-30]. However, it is still to be shown whether full-length Mical1 binds to two Rab molecules and if there is any allosteric interaction between the two binding sites.

In this study, we comprehensively characterized the auto-inhibited and active states of human Mical1 using biochemical and structural methods. Via isothermal titration calorimetry (ITC), we confirmed that the N-terminal MO-CH-LIM domains interact with the C-terminal bMERB domain, requiring the full-length bMERB domain for this interaction. Crosslinking-mass spectrometry (XL-MS) experiments supported the auto-inhibited state of Mical1. Utilizing AlphaFold2[31], we constructed a model revealing the auto-inhibited state and identified crucial interacting residues. Additionally, we confirmed the 1:2 stoichiometry of Rab8a binding to full-length Mical1. Next, we investigated whether allostery exists in the N- and C-terminal Rab binding sites. To answer this, we have used the bMERB domain, since it shows similar Rab affinity as full-length Mical1. Biochemical experiments show that Rab8 first binds to the high-affinity C-terminal site, facilitating subsequent second Rab8 binding to the low-affinity N-terminal site. These findings underscore the essential role of Rab binding in Mical1 activation.

Results and Discussion

Mical1 exists in an auto-inhibited state

Human Mical1 comprises four domains: an N-terminal monooxygenase (MO), a central calponin (CH), a LIM (Lin-11, Isl-1, and Mec-3) domain, and a C-terminal bivalent Mical/EHBP Rab-binding (bMERB) domain. Domain boundaries are taken from isoform 1 (UniProt ID: Q8TDZ2) (Supplementary Fig. 1). To characterize the auto-inhibited and active states, we purified full-length Mical1 and various deletion constructs (Fig. 1a and Supplementary Table. 2). All constructs except the bMERB domain are tagged with a C-terminal histidine tag. Further, to determine the oligomeric states of the proteins, their native masses were determined by size exclusion chromatography combined with multi-angle light scattering analysis (SEC-MALS). Results showed that all the purified constructs predominantly

95 exist as monomers. The average molar masses were as follows: full-length Mical1, 112.2 kDa
96 (theoretical mass: 118.94 kDa); MO-CH-LIM (residues 1-781), 86.2 kDa (theoretical mass: 86.48 kDa);
97 MO-CH (residues 1-615), 69.4 kDa (theoretical mass: 68.23 kDa); MO (residues 1-488), 55.78 kDa
98 (theoretical mass: 55.14 kDa); bMERB (residues 918-1067), 18.13 kDa (theoretical mass: 17.83 kDa)
99 (Fig. 1b-f).

100 Several studies have indicated that, in the absence of Rab, the bMERB domain forms an intramolecular
101 interaction with the other domains (CH/LIM/MO-CH-LIM)[26,32-35]. Full-length Mical is catalytically
102 inactive, with its enzyme activity somehow inhibited by the C-terminal domain[36]. Fremont *et al*.,
103 proposed a Mical1 auto-inhibition model based on F-actin depolymerization assays and cell biology
104 data, suggesting that the N-terminal monooxygenase and CH and LIM domains (MO-CH-LIM) interact
105 with the bMERB domain to form an inactive complex[26]. The binding of Rab releases auto-inhibition,
106 resulting in F-actin depolymerization[26,36,37]. However, the biochemistry of the auto-inhibited state is
107 not well understood. Therefore, we aimed to confirm and quantify the intramolecular interaction
108 between the N- and C-terminal domains of Mical1 by investigating the interaction between the
109 separately purified C-terminal bMERB domain and the N-terminal MO/MO-CH/MO-CH-LIM domains
110 via ITC. We observed binding between the MO-CH-LIM domain construct and the bMERB domain,
111 driven by enthalpy with a K_D value of 2.7 ± 0.16 µM and a 1:1 stoichiometry. However, no binding was
112 observed between the isolated bMERB domain and the MO-CH/MO domains (Fig. 1g-i). Our previous
113 work also showed that the Mical1 CH-LIM construct and isolated CH and LIM domains do not interact
114 with the bMERB domain[30]. Thus, our data indicate that all three domains (MO-CH-LIM) are necessary
115 for stable bMERB interaction (Fig. 1g-i). Like Mical1, other F-actin interacting proteins, such as Myosin
116 V, Talin2, and Vinculin, also exist in an auto-inhibited state, with their activation being spatially and
117 temporally regulated[38,39].

118 **Full-length bMERB domain is essential for MO-CH-LIM interaction**

119 Mical1 and Mical3, among other bMERB family members, feature a high-affinity C-terminal Rab-
120 binding site (Ct-RBS2; helices 2-3) and a lower-affinity N-terminal site (Nt-RBS1; helices 1-2). In
121 contrast, EHBP1L1's bMERB domain has two Rab-binding sites of similar affinities[28,29]. EHBP1, another
122 family member, has a single Rab-binding site and forms an auto-inhibited complex where helices 1-2
123 of the bMERB domain constitute the CH binding site, with Rab binding at the C-terminal site (helices
124 2-3) releasing auto-inhibition[30]. To pinpoint the exact binding site on Mical1, we generated two
125 deletion constructs of its bMERB domain, deleting either the N-terminal or C-terminal helix, and tested
126 their interaction with MO-CH-LIM. Our ITC data confirm that the full-length bMERB domain is
127 necessary for a stable interaction, as the deletion constructs did not form a stable complex. (Fig. 2a-
128 c).

129 To independently verify the interaction between the MO-CH-LIM and bMERB domains, we performed
130 crosslinking mass spectrometry (XL-MS) analyses. Two experiments were conducted: first, using full-
131 length Mical1; second, mixing the MO-CH-LIM construct and the bMERB domain in a 1:2 ratio to
132 achieve a saturated MO-CH-LIM complex. (Fig. 2d-f). A total of 59 peptides were identified from Mical1
133 full-length experiments, and 76 peptides were identified from the MO-CH-LIM:bMERB complex.
134 Crosslink mapping revealed numerous reproducible inter-domain and intra-domain connections
135 between the two experiments. In the Mical1 full-length experiment, 6 peptides linked MO and bMERB
136 domains, compared to 24 peptides in the MO-CH-LIM:bMERB complex experiment, confirming the
137 interaction between the full-length bMERB domain and MO. This aligns with our ITC data, indicating
138 the involvement of all three bMERB helices. However, no cross-links were found between CH and
139 bMERB or LIM and bMERB domains. Our ITC results clearly demonstrate that the MO-CH-LIM
140 construct interacts with the bMERB domain but not with MO or MO-CH. The absence of cross-links
141 may be due to the limited number of lysine residues in the CH and LIM domains (2 in CH, 1 in LIM),
142 potentially indicating they are not part of the binding interface. Nevertheless, XL-MS experiments
143 suggest that the bMERB domain interacts with the MO domain, implying the formation of an
144 intramolecular complex.

145 **Structural basis of Mical1 auto-inhibition**

146 To understand the molecular basis of the MO-CH-LIM:bMERB interaction, we utilized AlphaFold2[31]
147 modeling to predict the auto-inhibited state of Mical1, producing a model with high confidence
148 predicted local difference distance test (pLDDT) scores and predicted alignment errors (PAE), which
149 we analyzed in detail (Fig. 3a and Supplementary Fig. 2).

150 The AlphaFold2 model predicts that the MO (residues 1-488), CH (residues 508-613), Helix^{CHL} (residues
151 624-654), LIM (residues 692-751) domains, and linker (residues 800-855) interact with the C-terminal
152 bMERB (residues 886-1067) domain, forming an auto-inhibited complex. Helices 1-2 of the bMERB
153 domain interact with the MO, CH, and LIM domains, while helix 3 specifically interacts with Helix^{CHL},
154 resulting in three distinct binding interfaces on the bMERB domain, predominantly through
155 hydrophobic interactions (Fig. 3a-c). The first binding interface involves the first half of helix 1 and the
156 second half of helix 2 of the bMERB domain, where the MO domain interacts (1190 Å^2 buried surface).
157 The MO domain consists of two core domains: a large domain (MO^{Large_domain}, residues 1–226 and 374–
158 484) and a smaller cap domain (MO^{Cap_domain}, residues 235–366). Both domains are connected by β-
159 strands β9 (residues 228–234) and β15 (residues 367–373). The active site is a cleft formed by both
160 the MO^{Large_domain} and the MO^{Cap_domain}, containing a FAD molecule. Both the MO^{Large_domain} and the
161 MO^{Cap_domain} interact with the bMERB domain. The MO^{Large_domain} interacts with helix 1, whereas the
162 MO^{Cap_domain} interacts with both helices 1 and 2 (Fig. 3d,e). The binding site is opposite to the active

site (FAD binding cleft). The second binding interface involves the center of the bMERB domain, where all three helices interact with the MO^{Cap_domain}, LIM domain, and $Helix^{CHL}$. The third binding interface centers on helices 1-2 of the bMERB domain, facilitating interactions between the CH (507 Å²) and LIM (652 Å²) domains (Fig. 3f). While helix 3 of the bMERB domain does not directly interact with the MO, CH, and LIM domains, our ITC data indicate its necessity for complex formation. This necessity is likely due to stabilizing interactions between helices 2 and 3 and the $Helix^{CHL}$, suggesting that this interaction stabilizes the second binding interface where the MO and LIM domains interact with helices 1 and 2 of the bMERB domain (Fig. 3a).

Apart from the active site cleft, a smaller cleft is formed between the MO^{Large_domain} and MO^{Cap_domain}, occupied by helix 1 of the bMERB domain (Fig. 3d). This cleft includes loops connecting β9-β10, β17-α15, and β15 of the MO^{Large_domain}, and β11 and the loop connecting α10-11 of the MO^{Cap_domain}. Helix 1 residue K918 forms hydrogen bonds with D153 and E257 of the MO domain, while E921 interacts with S259 of the MO domain (Fig. 3a, inset1). The side chain of F925 of the bMERB domain inserts itself into a hydrophobic patch formed by P401, L402, and V285 residues of the MO domain. Similarly, I264 of the MO^{Cap_domain} inserts into the hydrophobic patch involving helix 1 (I931) and helix 2 (V995 and L998), while Y265 of the MO^{Cap_domain} interacts hydrophobically with F925 (Fig. 3a, inset1). Additionally, K235 in the β9-β10 loop forms a hydrogen bond with E939 (Fig. 3a, inset4)

The CH and LIM domain binding sites on the bMERB domain span the C-terminal half of helix 1 and the N-terminal half of helix 2, characterized by a hydrophobic array. $L598^{CH}$ interacts hydrophobically with L956, V971, and L974 of the bMERB domain, whereas $I601^{CH}$ similarly engages with L975 and V978. Further, the CH:bMERB interaction is reinforced by hydrogen bonds between residues $D596^{CH}$-R957 and $E512^{CH}$-K988 (Fig. 3a, inset2). V632 and F634 of $Helix^{CHL}$ interact hydrophobically with V985, I993, L1047, and F1050 of the bMERB domain (Fig. 3a, inset5). The LIM domain also engages extensively with the bMERB domain through hydrophobic interactions: $Y705^{LIM}$ with V950 and L954, $L707^{LIM}$ in the groove formed by L974, L977, and V978, and $W732^{LIM}$ with L935 and M992. Additionally, hydrogen bonds are observed between $R719^{LIM}$-E988 and $T730^{LIM}$-E939 (Fig. 3a, inset3-4).

Next, we compared the auto-inhibited Mical1 model with previously published crystal structures of Mical1 individual domains[26,40-42]. The predicted MO domain closely resembles the isolated mouse Mical1 MO domain in both oxidized (PDB: 2BRY) and reduced states (PDB: 2C4C)[40], with RMSD values of 0.299 Å for 396 Cα residues and 0.581 Å for 422 Cα residues, respectively (Supplementary Fig. 3a-b). Although the AlphaFold model lacks FAD, its active site residues are similar to the oxidized state of the mouse Mical1 MO domain (Fig. 3e). Even in the auto-inhibited state, the active site is accessible for catalysis. Previous studies have shown that in the reduced state of the MO domain, the FAD

196 isoalloxazine ring flips during the catalytic cycle, leading to conformational changes in active site
197 residues[40]. FAD's isoalloxazine ring flips during the catalytic cycle in the reduced MO domain, causing
198 changes in active site residues such as F399, W400, and P401 upon NADPH binding (Fig. 3d-e). F399,
199 in particular, undergoes significant changes upon NADPH binding. In the auto-inhibited AlphaFold2
200 model, bMERB domain binding sterically hinders this rotation, stabilizing the oxidized MO domain and
201 preventing the FAD transition to the reduced state (Fig. 3d-e). In the auto-inhibited state, the side
202 chains of I264 and Y265 in the MO^{Cap_domain} are inserted into a hydrophobic patch formed by helices 1
203 and 2 of the bMERB domain. In the isolated oxidized/reduced mouse MO domain structure, Y265 and
204 I264 lacked electron density, indicating that bMERB binding likely stabilizes the loop conformation of
205 the MO domain (Fig. 3d-e).

206 Furthermore, structural analysis of isolated human CH (PDB: 2DK9) and bMERB domain (PDB: 5LE0)
207 revealed differences from the AlphaFold2 predictions, with RMSD values of 1.089 Å for 92 Cα residues
208 in the CH domain and 0.967 Å for 94 Cα residues in the bMERB domain[26,41]. Notably, the maximum
209 structural difference was observed for the isolated human LIM domain (PDB: 2CO8), with an rmsd of
210 2.135 Å for 65 Cα residues[42] (Supplementary Fig. 3c-f). We hypothesize that the bMERB domain first
211 interacts with the CH domain, establishing the binding interface for the LIM domain. As the LIM
212 domain binds, it brings all three domains together, stabilizing the MO binding interface and forming a
213 compact structure. Finally, the MO domain interacts with both the bMERB and LIM domains,
214 facilitating the formation of a tightly packed auto-inhibited complex.

215 **Generation of bMERB interface mutants**

216 To corroborate the Mical1 auto-inhibited AlphaFold2 model, we conducted biochemical experiments.
217 Sequence alignment of bMERB domains reveals that surface residues interacting with MO-CH-LIM are
218 highly conserved across mammalian homologs (Supplementary Fig. 4). To assess the significance of
219 individual interface residues, we introduced mutations into each helix of the bMERB domain based on
220 the AlphaFold2 Mical1 auto-inhibited model and analyzed their interaction with MO-CH-LIM using ITC
221 experiments. (Fig. 4). All bMERB mutants with alanine substitutions at conserved residues, except
222 K918A_E921A, show a significant decrease in binding affinity. The K918A and E921A double mutations
223 in helix 1 reduce affinity for MO-CH-LIM by only 2-fold (Fig. 4c). K918 forms hydrogen bonds with D153
224 and E257 of the MO domain, while E921 bonds with S259. In contrast, mutation of F925 abrogates the
225 MO-CH-LIM interaction (Fig. 4d), as its side chain inserts into the hydrophobic pocket formed by A262,
226 Y265, and V285 of the MO domain. The E939A mutant shows more than a 5-fold reduction in binding
227 affinity with MO-CH-LIM (Fig. 4e). The side chain of E939 forms hydrogen bonds with K235 of the MO
228 domain and T730 in the LIM domain.

229 Double alanine mutations in helix 2 (L974A_L975A and L977A_V978A) lead to a 6-fold reduction in
230 binding affinity (Fig. 4f, g). Residues L956, V971, L974, L975, L977, and V978 of the bMERB domain
231 form a hydrophobic patch that accommodates the CH and LIM domains. The side chain of L598 in the
232 CH domain fits into the hydrophobic pocket formed by L956, V971, and L974, while I601 interacts with
233 V971 and L975. Additionally, L707 of the LIM domain forms a hydrophobic interaction with L974, L977,
234 and V978 of the bMERB domain. The M992A_I993A double alanine mutant in helix 2 causes a more
235 than 25-fold reduction in binding affinity (Fig. 4h). M992 interacts with LIM domain residue W732, and
236 I993 interacts with F634 of $Helix^{CHL}$ (residues 624-654).

237 Furthermore, mutating residues L1047 and F1050 of helix 3 to alanine eliminates detectable binding
238 with MO-CH-LIM (Fig. 4i). Notably, L1047 and F1050 interact with $Helix^{CHL}$ (residues 624-654), not with
239 MO, CH, or LIM domains. The side chain of F634 of $Helix^{CHL}$ inserts into a hydrophobic patch formed
240 by I993 (helix 1), L1047, and F1050 (helix 2) of the bMERB domain, while V632 of $Helix^{CHL}$ interacts
241 with V985 of bMERB. The L1047 and F1050 mutations destabilize this hydrophobic patch.

242 **Allostery between the two Rab binding site**

243 We previously demonstrated that the Mical1 bMERB domain binds Rab8 in a 1:2 stoichiometry, with
244 helices 1-2 forming the low-affinity N-terminal binding site (Nt-RBS1) and helices 2-3 forming the high-
245 affinity C-terminal binding site (Ct-RBS2)[28]. Deleting either the N- or C-terminal helix resulted in
246 binding Rab molecules at a 1:1 stoichiometry[28]. We investigated whether two Rab molecules bind to
247 the bMERB domain of full-length Mical1 and as expected full-length Mical1 binds Rab8 with a 1:2
248 stoichiometry, similar to the isolated bMERB domain, but with slightly lower affinity (K_{D1}: 40 vs. 10 nM
249 and K_{D2}: 0.73 vs. 1.12 µM) (Fig. 5a-b). Next, we examined whether the binding of a Rab molecule at
250 either the N- or C-terminal site affects the binding of a second Rab molecule at the other site, or if the
251 two sites operate independently. Since full-length Mical1 exhibits a similar range of Rab8 binding
252 affinities as the isolated bMERB domain (Fig. 5b, h), we generated and purified isolated bMERB domain
253 mutants based on the bMERB:Rab10 complex (PDB: 5LPN)[28] structure (Fig. 5c). We assessed their
254 interaction with Rab8 by varying the bMERB:Rab ratio (1:1.1 and 1:2.2) using analytical size exclusion
255 chromatography. These experiments aimed to identify constructs that either show no or defective
256 complex formation or fail to display an increase in complex formation upon increasing the Rab
257 concentration. Furthermore, the stoichiometry of the complex was determined using isothermal
258 titration calorimetry (ITC) with selective constructs.

259 First, we generated mutants targeting Nt-RBS1. Mutants K918A_E921A, F925A, W970A, and
260 L974A_L975A showed no binding defects (Supplementary Fig. 5a-d, h). However, E939A and L956S
261 exhibited only a slight increase in complex formation at higher bMERB ratios (1:1.1 to 1:2.2), indicating

262 a lower affinity for the second N-terminal Rab binding (Supplementary Fig. 5e, f). Mutants
263 L977A_V978A, V978A_V985A, V978A, V985A, M992A_I993A, and L1047A_F1050A showed no
264 significant change in complex formation with increased Rab concentration, suggesting either 1:1
265 binding or defective binding at both sites (Supplementary Fig. 5i-n).

266 We next generated mutants targeting Ct-RBS2. Mutants L1011S and V1038A showed no apparent
267 defects (Supplementary Fig. 6a-d). However, mutants V1041A, R1044A, and I1048A formed smaller
268 complexes on aSEC and showed no significant change in complex formation with varying Rab
269 concentrations, suggesting binding defects (Supplementary Fig. 6e-g). Notably, the double mutant
270 V1041A_I1048A showed minimal complex formation, indicating that these mutations affect binding
271 at both Rab sites (Supplementary Fig. 6h).

272 Distinct heat exchange patterns for Rab binding at the N-terminal and C-terminal sites of Mical1 were
273 previously observed, with C-terminal binding being enthalpy-driven and N-terminal binding entropy-
274 driven[28]. To precisely determine the impact of specific mutations on Rab binding, we conducted ITC
275 experiments with mutants: $bMERB_{V978A_V985A}$, $bMERB_{V1041A_I1048A}$, $bMERB_{M992A_I993A}$, and
276 $bMERB_{L1047A_F1050A}$. The ITC data unequivocally demonstrate that $bMERB_{V978A_V985A}$ binds to Rab8 with a
277 1:1 stoichiometry, an enthalpy-driven reaction, and affinity similar to Ct-RBS2. In contrast,
278 $bMERB_{V1041A_I1048A}$ exhibited low heat exchange and cannot be reliably fitted, indicating that C-terminal
279 binding is necessary for Rab binding at the N-terminal site (Fig. 5h-l). Residues V978/V985 and
280 V1041/I1048 are functionally equivalent, interacting with specific Rab10 residues (I44, W63, F46 for
281 V978/V1041; L9, F46A, I48 for V985/I1048) (Fig. 5c, Insets 1-2). V978 and V985 are crucial for N-
282 terminal Rab binding, as single mutants V978A and V985A show similar binding as of the double
283 mutant V978A_V985A. Conversely, the double mutant V1041A_I1048A exhibits a pronounced effect
284 on Rab10 binding compared to individual mutants V1041A and I1048A, indicating that perturbations
285 in the N-terminal binding site still allow Rab8 to bind to the C-terminal site, whereas perturbations at
286 Ct-RBS2 also affect binding at Nt-RBS1. This suggests a sequential binding mechanism for Rabs. To
287 further support our observation, we performed SEC experiments with V978A_V985A and
288 V1041A_I1048A bMERB mutants with other Rab8 family members (Rab10, Rab13, and Rab15). Similar
289 observations were made; however, compared to Rab8, Rab10 showed a lesser increase in complex
290 formation upon increasing the bMERB:Rab ratio, suggesting a slightly lower affinity for the N-terminal
291 Rab binding (Supplementary Fig. 7).

292 The other Nt-RBS1 mutant, $bMERB_{M992A_I993A}$, exhibited a similar high affinity for C-terminal Rab8
293 binding, while a more than 30-fold decrease in N-terminal Rab binding was observed. The residue
294 M992 forms hydrophobic interactions with Y6 of Rab10 (Nt-RBS1) (Fig. 5o, Inset3). An intriguing

295 observation arose with the mutant bMERB$_{L1047A_F1050A}$, which demonstrated reduced binding affinity
296 for both Rab binding sites. This mutant showed over a 20-fold decrease in C-terminal Rab8 binding
297 and a 10-fold reduction in N-terminal Rab binding (Fig. 5p). Residues L1047 and F1050 contribute to
298 hydrophobic interactions with L8 of Rab10 (Nt-RBS1) (Fig. 5c, Inset3). However, L1047 and F1050 do
299 not participate in binding with Rab10 at Ct-RBS2; the decrease in binding affinity might be due to a
300 change in local hydrophobicity, as these residues lie on the opposite side of the crucial I1048.
301 Previously, we reported that the N-terminus of the Rab8 family member provides specificity[28]. L8^{Rab10}
302 is implicated in the RabSF1 interaction with L1047 and F1050, thereby further stabilizing the
303 interaction. These findings suggest that the conformation of helix 3 of the bMERB domain plays a
304 crucial role in Rab binding at both the N-terminal and C-terminal Rab binding sites within the full-
305 length bMERB domain background. This contrasts with earlier findings showing that Rab8 bound to N-
306 and C-terminal helix-deleted constructs in a 1:1 ratio, suggesting site independence[28].

307 We propose that the absence of helix 3 may cause helices 1-2 to adopt a different conformation,
308 accommodating the Rab molecule. Overall, our data suggest allosteric communication between the
309 N-terminal and C-terminal Rab binding sites, with the first Rab molecule binding at Ct-RBS2, followed
310 by the second Rab molecule binding at Nt-RBS1.

311 **The overall structure of the bMERB$_{V978A_V985}$:Rab10/bMERB$_{V978A}$:Rab10 complex**

312 To gain mechanistic insight, we attempted to crystallize bMERB$_{V978A_V985}$:Rab10, bMERB$_{V978A}$:Rab10,
313 bMERB$_{V985A}$:Rab10 complexes, and the bMERB$_{V1041A_I1048A}$ domain. We successfully obtained well-
314 diffracting crystals of the bMERB$_{V978A_V985}$:Rab10 and bMERB$_{V978A}$:Rab10 complexes, with space group
315 $P2_1$, diffracting to 1.8 and 2.05 Å, respectively. Structures were solved as described in the materials
316 and methods (Data and refinement statistics are in Supplementary Table 1).

317 The asymmetric unit contained a single copy of either the bMERB$_{V978A_V985A}$:Rab10 or
318 bMERB$_{V978A}$:Rab10 complex. Both structures are nearly identical (Fig. 6a and Supplementary Fig. 8**)**, so
319 here we describe the bMERB$_{V978A_V985A}$:Rab10 complex structure in detail. In accordance with our aSEC
320 and ITC data, a single molecule of Rab10 was bound to the C-terminal Rab binding site. Structural
321 alignment of bMERB$_{V978A_V985A}$:Rab10 with the wild-type bMERB:Rab10 (PDB: 5LPN)[28] shows that the
322 C-terminal Rab binding site of the mutant bMERB domain adopts the same conformation as the wild-
323 type complex. However, the second half of helix 2 of the mutant bMERB domain adopts a different
324 conformation. The N-terminal Rab binding site is formed by a kink in the second half of helix 2 and the
325 movement of the first half of helix 1 towards Rab. In the bMERB$_{V978A_V985A}$:Rab10 structure, the second
326 helix's conformation is similar to the unbound bMERB domain conformation (PDB: 5LEO)[26] (Fig. 6b-c).

327 This mutation of V978 or V985 leads to the abrogation of the second Rab binding at the N-terminal
328 Rab binding site, as found in aSEC/ITC experiments as well.

329 **Phosphomimetic mutation of S960 of the bMERB domain**

330 Recently, Macgarry *et al*., proposed an alternate mode of Mical1 activation by Rho GTPases and
331 showed that upon extracellular ligand stimulation, Cdc42 interacts with its effector PAK1 and active
332 Cdc42:PAK1 then binds to the MO domain of Mical1, PAK1, a serine/threonine kinase, phosphorylates
333 S817 and S960 of the Mical1 bMERB domain[43]. The authors proposed that this phosphorylation
334 enhances Rab10 binding, which activates Mical1 and increases F-actin disassembly[43]. We analyzed
335 AlphaFold2 model and found that S817 lies in the linker region, while S960 is part of the bMERB
336 domain. Despite the low pLDDT score for this linker region, the position of S817 is highly reproducible
337 across models, and the side chain is pointing towards a negatively charged patch. Phosphorylation
338 might induce charge repulsion, potentially 'loosening' the auto-inhibited complex (Fig. 7a-b and
339 Supplementary Fig. 9). However, further biochemical and structural validation is needed.

340 Previously, we showed that the bMERB domain interacts with Rab8, Rab10, Rab13, and Rab15, but
341 lacked quantitative binding data. We have now quantified these interactions. Similar to Rab8, ITC data
342 reveal that Rab10 and Rab15 bind to the bMERB domain in a 1:2 stoichiometry, with one high-affinity
343 site (Ct-RBS2: 11 nM for Rab10, 2.5 nM for Rab15; enthalpy-driven) and one low-affinity site (Nt-RBS1:
344 3.73 µM for Rab10, 2.91 µM for Rab15; entropy-driven). We purified the $bMERB_{S960D}$ mutant and
345 assessed its interaction with Rab8, Rab10, and Rab15 using aSEC/ITC. The phosphomimetic mutation
346 at S960 did not affect Rab binding, consistent with our structural observations that S960, located in
347 helix 1 of the Nt-RBS1 site, does not interact with Rab10 (Fig. 7c-o).

348 Based on our findings, we propose that phosphorylation of both S817 and S960 may facilitate the
349 release of auto-inhibition in Mical1, exposing the bMERB domain for Rab binding without affecting
350 Rab affinity. Further biochemical studies are needed to fully elucidate the activation mechanism of
351 Mical1 by the RhoGTPase-PAK1 pathway.

352 **Impact of Rab binding site mutations in the bMERB domain on MO-CH-LIM interaction**

353 In the absence of Rab, the Nt-RBS1 of bMERB accommodates the CH and LIM domain, so we
354 investigated the effect of several RBS mutants of the bMERB domain on MO-CH-LIM interaction (Fig.
355 8). The L956S mutant displayed more than a 9-fold reduction in binding affinity (Fig. 8c). L956 forms a
356 hydrophobic interaction with L598 of the CH domain; however, it is also part of a continuous array of
357 hydrophobic residues. Therefore, we propose that this mutation may lead to the destabilization of the
358 hydrophobic patch. In contrast, the phosphomimetic mutant S960D did not affect MO-CH-LIM binding,
359 as this residue is not part of the predicted binding interface (Fig. 8d). Another putatively non-

360 interacting residue, the W970A mutant, exhibited a 4-fold decrease in binding affinity (Fig. 8e).
361 Although W970^{bMERB} is not directly involved in the interaction, it may contribute to stabilizing the
362 hydrophobic patch of the bMERB domain, which is crucial for MO-CH-LIM interaction.

363 The double alanine mutations V978A_V985A completely abolished the MO-CH-LIM interaction (Fig.
364 8f). Interestingly, single mutations V978A and V985A caused a 2-fold and 10-fold reduction in binding
365 affinity, respectively (Fig. 8g-h). V978 interacts with A602 of the CH domain and L707 of the LIM
366 domain, while V985 interacts with V632 of the Helix^{CHL}. This indicates that the hydrophobic nature of
367 these residues is crucial for stabilizing CH and LIM interactions with the bMERB domain. In contrast,
368 double alanine mutations of non-interface residues, V1041A_I1048A, showed slightly better affinity
369 than the wild type (Fig. 8i).

370 **Structural basis of Mical1 activation**

371 To unravel the structural basis for the release of the MO, CH, and LIM domains from the bMERB
372 domain upon Rab binding, we superimposed the Mical1 auto-inhibited AlphaFold2 model with the
373 bMERB:Rab10 complex (PDB: 5LPN) structure[28]. Superimposition reveals that in the auto-inhibited
374 Mical1 model, the Nt-RBS1 site is blocked by the CH and LIM domains, along with Helix^{CHL}. Upon Rab
375 binding, the bMERB domain helices undergo significant conformational changes (Fig. 9a-c). Helix 3
376 adopts a new conformation that interferes with the CH domain and Helix^{CHL}. Meanwhile, binding of
377 the second Rab molecule shifts helices 1-2 towards the Rab, further disrupting the interaction with
378 the CH domain.

379 The AlphaFold2 auto-inhibited model suggests that while the active site is accessible, helix 1 of the
380 bMERB domain restricts the catalytic loop (amino acids 395-405) movement (Fig. 3e). Conformational
381 changes in W400 stabilize FAD binding via π-π stacking and may facilitate hydride transfer from NADPH
382 to FAD[40]. Several studies suggest that during oxidation, methionine residues approach W400, making
383 them accessible to hydrogen peroxide[40,44]. The AlphaFold2 model indicates that enzyme activity is
384 likely inhibited by the bMERB domain, which restricts the movement of the catalytic loop (Fig. 3e). In
385 the Mical1 auto-inhibited model, F399's movement is restricted, and the MO domain conformation
386 resembles that of the isolated MO domain in the oxidized state (PDB: 2BRY) (Fig. 3e).

387 Next, we propose a model for Mical1 activation (Fig. 10). Comparing the Mical1 auto-inhibited state
388 with the bMERB complex reveals that Nt-RBS1 is blocked by the CH, Helix^{CHL}, and LIM domains.
389 However, helix 3 of the bMERB domain is accessible, allowing the first Rab8 molecule to bind at the
390 C-terminal high-affinity Rab binding site, defining the helix 3 conformation. This binding displaces the
391 CH domain and Helix^{CHL}, loosening the structure and exposing Nt-RBS1. A second Rab molecule then
392 binds at the low-affinity RBS, preventing the reassembly of the bMERB:CH domain. The binding

393 induces significant conformational changes in helices 1 and 2, disrupting their interaction with the MO
394 domain. Key residues E939, F925, and N999 in helices 1 and 2 shift side chain orientations, leading to
395 MO domain dissociation (Fig. 9d), supported by ITC data. These movements also further dissociate the
396 LIM domain. Consequently, the binding of the second Rab molecule relieves auto-inhibition, allowing
397 access to the MO, CH, and LIM domains. The active MO domain then induces F-actin depolymerization.

398 Mical1 regulates actin dynamics by selectively oxidizing Met44 and Met47 of F-actin in an NADPH-
399 dependent manner, causing depolymerization and severing of F-actin[6,45,46,49]. We have previously
400 shown that Mical1's CH, LIM, or CH-LIM domain fails to interact with F-actin [30]. The Mical1 CH domain
401 is structurally similar to CH type-2 domains, which cannot directly bind to F-actin, unlike CH type-1
402 domains. We tested full-length Mical1, MO-CH-LIM, MO-CH, and MO constructs for F-actin interaction
403 using actin co-sedimentation assays. The results showed that MO-CH-LIM, MO-CH, and MO constructs
404 interact with F-actin, indicating the MO domain is essential and sufficient for this interaction. Full-
405 length Mical1 showed less interaction, suggesting that Rab binding is needed to overcome auto-
406 inhibition for F-actin binding (Fig. 9e).

407 Previously, we suggested that the binding of two Rab molecules to Mical1 could increase the local
408 concentration of specific Rab molecules, creating Rab microdomains and controlling Mical1 activity.
409 Based on our data, we now propose that the initial binding of the first Rab molecule to a high-affinity
410 site recruits Mical1 to specific membranes and alleviates its auto-inhibited state. This facilitates the
411 subsequent binding of the second Rab molecule at the low-affinity Nt-RBS1 site, further stabilizing
412 Mical1's active state by preventing the rebinding of the MO, CH, and LIM domains. This process
413 regulates the duration of enzyme activity and thus F-actin dynamics (Fig. 10). For Mical-like proteins,
414 a concerted Rab recruitment cascade has been reported. For instance, Mical-L1 connects Rab35 and
415 Rab8. Another study demonstrated that Mical-L1 is recruited to recycling endosomes by Rab35, which
416 subsequently recruits other Rab proteins such as Rab8, Rab13, and Rab36[50]. Similarly, in Mical1-L2-
417 dependent GLUT4 translocation, trafficking relies on the concerted action of Rab8 and Rab13[51]. The
418 authors suggested that bMERB domain dimerization allows for concerted recruitment; however, in
419 the case of Mical1, a single bMERB domain can recruit Rab proteins in a concerted manner.

420 In conclusion, our study has provided biochemical and structural insights into both the auto-inhibited
421 and active states of Mical1. Our data offer a detailed overview of the MO-CH-LIM:bMERB interaction,
422 with mutagenesis experiments highlighting the crucial residues involved. Additionally, we have
423 elucidated the activation mechanism of Mical1, presenting evidence of allosteric regulation between
424 the two Rab binding sites and identifying the key residues required for Rab recruitment.

425 # Methods

426 ## Plasmid cloning

427 All expression constructs were generated by standard cloning techniques, using Phusion polymerase,
428 restriction digestion, and ligation by T4 DNA ligase, and point mutants were generated by quick-
429 change site-directed mutagenesis, using Phusion polymerase. All plasmids were verified by Sanger
430 sequencing. The bacterial expression constructs for Mical1, MO-CH-LIM, MO-CH, and MO were
431 previously described[52]. A detailed overview of all expression vectors employed in this study is
432 presented in Supplementary Table 2.

433 ## Recombinant protein expression and purification

434 Human Mical1 full-length and truncated C-terminal His6-tagged versions of MO, MO-CH, and MO-CH-
435 LIM domains were expressed and purified with a modified protocol as described previously[52]. Proteins
436 were recombinantly expressed in *E. coli* Rosetta (DE3) (Merck Millipore) cells in LB media
437 supplemented with Ampicillin (125 µg/mL) and Chloramphenicol (34 µg/mL) and cells were grown at
438 37°C to OD_{600} nm = 0.8–1.0 and stored at 4°C for 30 min. Expression was induced by the addition of
439 0.5 mM IPTG, and cells were allowed to grow at 19°C for 14-16 hr. Cells were pelleted and stored at -
440 80°C until ready for purification. Cells were mechanically lysed by passing through a fluidizer
441 (Microfluidic**)** in a buffer [Buffer A: 50 mM Hepes pH 8.0, 500 mM NaCl, 2 mM βME (2-
442 Mercaptoethanol), 1 mM PMSF (Phenylmethylsulfonyl fluoride) and 1 mM CHAPS (3-((3-
443 cholamidopropyl) dimethylammonio)-1-propanesulfonate)] and lysates were cleared by
444 centrifugation at 75,600 g at 4 °C for 30 min using a JA 25.50 rotor (Beckman-Coulter). Next, the
445 proteins were purified by Ni^{2+}-affinity chromatography, and protein fractions were eluted with an
446 imidazole gradient (Buffer B: buffer A supplemented with 500 mM imidazole pH 8.0). The His6-tagged
447 protein was overnight dialyzed at 4 °C in a buffer (50 mM Tris pH 8.0, 100 mM NaCl, and 2 mM βME).
448 Further purity was achieved by gel filtration (HiLoad Superdex 200 26/60, GE Healthcare) (Buffer:
449 20 mM Tris 8.0, 100 mM NaCl, and 2 mM DTE). Depending on purity, the protein was further purified
450 by one to three successive rounds of anion exchange chromatography (POROS™ 50 HQ strong anion
451 exchange resin; Thermo Scientific™). The purified protein was collected, concentrated, and washed
452 with final buffer (Storage buffer: 20 mM Tris pH 8.0, 100 mM NaCl, and 2 mM DTE) using Amicon®
453 Ultra-15 50K NMWL centrifugal filter devices; flash-frozen in liquid N_2 and stored at −80 °C. Protein
454 concentration was determined by using Bradford assay (Bio-Rad). Tag-free Mical1 full-length bMERB
455 domain, truncated bMERB domains, and mutants were purified as described previously[28].

456 Human Rab GTPases (tag-free) were expressed and purified as described previously[28]. Rabs were
457 preparatively loaded with GppNHp (Guanosine-5'-[β-γ-Imido]-triphosphate) and the reaction was

458 performed as described previously [28]. Nucleotide exchange efficiency was quantified by C18 reversed-
459 phase column (Prontosil C18, Bischoff Chromatography) with HPLC in 50 mM potassium phosphate
460 buffer pH 6.6, 10 mM tetrabutylammonium bromide and 12% acetonitrile (v/v). Protein samples were
461 heat precipitated at 95 °C for 5 min and centrifuged at 15700 g for 10 min and loaded (25 µM, 20 µL)
462 on the column. Peaks were integrated and to determine the nucleotide retention times; a nucleotide
463 standard run was performed. The purified protein was collected and concentrated; flash-frozen in
464 liquid N_2 and stored at −80 °C.

465 **Size exclusion chromatography coupled with multi-angle light scattering (SEC-MALS)**

466 Full-length Mical1, MO-CH-LIM, MO-CH, and MO domains were analyzed using a Superdex 200 10/30
467 GL column coupled with a multi-angle light scattering (MALS) instrument (Wyatt Technology). The
468 analysis was conducted in a buffer containing 20 mM Hepes pH 8.0, 50 mM NaCl, 1 mM $MgCl_2$, and 1
469 mM TCEP at 25 °C. The bMERB domain was analyzed using a Superdex 75 10/30 GL column coupled
470 with a MALS instrument (Wyatt Technology) in a buffer containing 20 mM Hepes pH 7.5, 50 mM NaCl,
471 1 mM $MgCl_2$, and 1 mM TCEP. The chromatography system was connected in series with a light-
472 scattering detector (Wyatt Dawn HELIOS II) and a refractive index detector (Wyatt Optilab t-rEX). BSA
473 (Sigma) was used as a standard to calibrate the system, and 20 µL of each sample (2 mg/mL) was
474 injected. Data analysis was performed with ASTRA 7.3.2 software (Wyatt Technology), yielding the
475 molar mass and mass distribution (polydispersity) of the samples.

476 **Analytical size exclusion chromatography (aSEC)**

477 The bMERB:GppNHp Rab ($Rab8a_{1-176}$, $Rab10_{1-175}$, $Rab13_{1-176}$, and $Rab15_{1-176}$) complex formation was
478 analyzed by analytical size exclusion chromatography (aSEC). 110 µM of bMERB domain and 121 µM
479 of GppNHp protein (Effector: Rab stoichiometry of 1: 1.1) were mixed in a buffer containing 20 mM
480 Hepes pH 7.5, 50 mM NaCl, 1 mM $MgCl_2$, and 2 mM DTE and centrifuged for 15 min at 15700 g at 4°C.
481 40 µL of the mixture was injected into a Superdex 75 10/300 GL gel filtration column (GE Healthcare)
482 pre-equilibrated with the Rab buffer with a flow rate of 0.5 mL/min at room temperature and
483 absorption at 280 nm was recorded.

484 **Isothermal titration calorimetry (ITC)**

485 Protein-protein interaction measurements were conducted by isothermal titration calorimetry (ITC)
486 using an ITC200 and PEAQ-ITC microcalorimeter (MicroCal). $Mical1_{fl}$/bMERB:Rab interaction
487 measurements were performed in the buffer containing 20 mM Hepes 7.5, 50 mM NaCl, 1 mM $MgCl_2$,
488 and 1 mM Tris (2-carboxymethyl) phosphine (TCEP) whereas MO-CH-LIM/MO-CH/MO:bMERB
489 interactions were performed in buffer containing 20 mM Hepes 8.0, 150 mM NaCl and 1 mM TCEP at
490 25°C. Wild types and mutant proteins were dialyzed overnight in their respective buffer. Samples were

491 centrifuged at 15700 g for 30 min at 4°C and protein concentration was determined by Bradford assay
492 (Bio-Rad). 600 µM of GppNHp Rab8a$_{1-176}$ was titrated into the cell containing 30 µM bMERB domain
493 and for full-length Mical1: Rab8 measurement, 800 µM of GppNHp Rab8a$_{1-176}$ was titrated into the cell
494 containing 40 µM full length Mical1. For MO-CH-LIM/MO-CH/MO:bMERB interaction 600 µM of
495 bMERB domain was titrated into the cell containing 30 µM MO-CH-LIM/MO-CH/MO domain. For the
496 control experiments, the buffer was titrated into the cell containing the protein of interest. In the
497 second control experiment, the protein in the syringe was titrated against the buffer. The binding
498 isotherms were integrated and corrected for the offset by subtracting the control experiment, and the
499 data were fitted to a one-site-binding or two-site-binding model using PEAQ-ITC software. The
500 reported ITC result is representative of one of at least three independent measurements.

501 **AlphaFold2 molecular modeling**

502 The Mical1 models (Mical1$_{fl}$ and MO-CH-LIM:bMERB complex) were generated using AlphaFold
503 multimer v2.3.1[31].

504 **Cross-linking experiment**

505 Full-length Mical1 (25 µM) was mixed with a 10-fold excess of freshly dissolved DSBU (disuccinimidyl
506 dibutyric urea; Thermo Fisher SCIENTIFIC, 50 mM stock) in DMSO in a cross-linking buffer (20 mM
507 Hepes, 100 mM NaCl, and 2 mM DTE). In a second experiment, 50 µM of MO-CH-LIM (residues 1-781)
508 was mixed with 100 µM of bMERB domain (residues 918-1067) in a final ratio of 1:2, respectively, and
509 again, 10 times DSBU was added in the crosslinking buffer. Samples were incubated at room
510 temperature for 1.30 hours, and the crosslinking reactions were quenched by the addition of 100 mM
511 Tris, pH 8.0. The samples were flash-frozen for further processing, as described previously[53]. Briefly,
512 the processing steps included the reduction of disulfide bonds using tris(2-carboxyethyl) phosphine,
513 alkylation of free thiol groups on cysteines with iodoacetamide, and proteolysis with trypsin. The
514 resulting peptides were enriched as described previously[54]. Briefly, the peptides were fractionated
515 using a Superdex™ 30 Increase 3.2/300 column in a buffer containing 50 mM ammonium acetate, 30%
516 acetonitrile, and 0.1% formic acid. Eluted samples were dried using a centrifugal evaporator and
517 stored at −20 °C until measurement.

518 **LC-MS/MS analysis**

519 LC-MS/MS analysis was performed as described previously[54]. Briefly, peptides were dissolved in 20 µL
520 of water containing 0.1% TFA. A total of 3 µL of this peptide solution were separated on an Ultimate
521 3000 RSLC nano system (precolumn: C18, Acclaim PepMap, 300 µm × 5 mm, 5 µm, 100 Å, separation
522 column: C18, Acclaim PepMap, 75 µm × 500 mm, 2 µm, 100 Å, Thermo Fisher Scientific). After loading
523 the sample on the pre-column, a multistep gradient from 5−40% B (90 min), 40−60% B (5 min), and

524 60−95% B (5 min) was used with a flow rate of 300 nL/min; solvent A: water + 0.1% formic acid; solvent
525 B: acetonitrile + 0.1% formic acid. The nano-HPLC system was coupled to a Q-Exactive Plus mass
526 spectrometer (Thermo Fisher Scientific). Data were acquired in data-dependent MS/MS mode. For full
527 scan MS, we used a mass range of m/z 300−1800, resolution of R = 140000 at m/z 200, one microscan
528 using an automated gain control (AGC) target of 3e6, and a maximum injection time (IT) of 50 ms.
529 Then, we acquired up to 10 HCD MS/MS scans of the most intense at least doubly charged ions
530 (resolution 17500, AGC target 1e5, IT 100 ms, isolation window 4.0 m/z, normalized collision energy
531 25.0, intensity threshold 2e4, dynamic exclusion 20.0 s). All spectra were recorded in profile mode.

532 **Data analysis and cross-link identification.**

533 Raw data from the Q-Exactive were converted to MGF (Mascot generic files) format with the program
534 msConvert GUI from ProteoWizard Toolkit version 3[55] and the mgf-files of all fractions of a crosslink
535 were merged into one file. Program MeroX version 2.0.1.4[56,57] was used for cross-link identification.
536 MS data in MGF format and protein sequences in FASTA format were loaded on the program and the
537 cross-linked residues were searched. In the settings, the precursor precision and the fragment ion
538 precision were set to 10.0 and 20.0 ppm, respectively. MS1 data were re-calibrated by 5 ppm
539 according to the average mass deviation of the raw MS data. The FDR was set to 50, i.e. no filtering
540 according to FDR with MeroX was done. RISEUP mode was used, and the maximum missing ions was
541 set to 1. Crosslinks data were exported to XiViewer[58].

542 **Crystallization and structure determination**

543 Initial crystallization condition screens for the protein complexes described in the paper were
544 performed using the JSG CORE I-IV, Pact, and Protein Complex suites (Qiagen). The sitting-drop vapor
545 diffusion method was employed, with a reservoir volume of 70 µL and a drop volume of 0.1 µL for the
546 protein (300 µM complexes, 1:1 Rab:effector) and 0.1 µL for the reservoir solution at 20°C. The best
547 conditions were then optimized using the sitting-drop vapor diffusion method, with varying drop sizes,
548 to obtain well-diffracting crystals. The complex of $bMERB_{V978A_V985A}$:$Rab10_{1-175}$ (300 µM of 1:1 complex)
549 was crystallized in 0.17 M Sodium acetate, 0.085 M Tris-HCl pH 8.5, 25.5% (w/v) PEG 4000 and 15%
550 (v/v) glycerol. The complex $bMERB_{V978A}$:$Rab10_{1-175}$ (300 µM of 1:1 complex) was crystallized in 0.1 M
551 Imidazole pH 8.0, 5% (w/v) PEG 3000 and 30% (v/v) PEG 200. Crystals were fished directly from the
552 crystallization drop and flash-cooled in liquid nitrogen. Diffraction data of $bMERB_{V978A_V985A}$:$Rab10_{1-175}$
553 was collected at 100 K on beamline X10SA at the Swiss Light Source (Paul Scherrer Institute, Villigen,
554 Switzerland). For the $bMERB_{V978A_V985A}$:$Rab10_{1-175}$ complex crystal, a native data set was collected at a
555 wavelength of 0.999968 Å. Whereas diffraction data of $bMERB_{V978A}$:$Rab10_{1-175}$ was collected at 100 K
556 on beamline ID23-2 at the European Synchrotron Radiation Facility (Grenoble, France). For the

557 bMERB$_{V978A}$:Rab10$_{1-175}$ complex crystal, a native data set was collected at a wavelength of 0.873130 Å.
558 Data were integrated and scaled with XDS[59].

559 The crystal of the bMERB$_{V978A_V985A}$:Rab10$_{1-175}$ complex diffracted to a resolution of 1.8 Å (space group
560 P2$_1$ with a = 53.673 Å, b = 48.807 Å, c = 79.199 Å), and a single copy of the complex is present in the
561 asymmetric unit of the crystal. The initial model for the bMERB$_{V978A_V985A}$:Rab10$_{1-175}$ complex was
562 obtained by molecular replacement using PHASER[60] with the crystal structure of the Mical1$_{bMERB}$:Rab
563 10 (PDB: 5LPN) as a search model[28]. The partial model was completed by manual building in Coot[61].
564 For the bMERB$_{V978A}$:Rab10$_{1-175}$ complex, the crystal diffracted to a resolution of 2.05 Å (space group
565 P2$_1$ with a = 53.517 Å, b = 49.434 Å, c = 79.095 Å), and one copy of the complex constitutes the
566 asymmetric unit of the crystal. The partial model was obtained by molecular replacement using
567 PHASER[60] and the bMERB$_{V978A_V985A}$:Rab10$_{1-175}$ was used as a search model. The initial model was
568 completed by manual building in Coot[61]. The final models were refined to convergence with
569 phenix.refine[62].

570 Data collection and refinement statistics are summarized in Supplementary Table 1. Structural figures
571 were prepared using PyMOL (DeLano Scientific; http://www.pymol.org).

572 **Actin co-sedimentation assay**

573 Rabbit skeletal muscle G-actin (AKL99) was purchased from Cytoskeleton. Inc and polymerized into F-
574 actin according to the manufacturer's protocol. F-actin (10 µM) was incubated for 1 hr at room
575 temperature (RT) with MO/MO-CH/MO-CH-LIM/Mical1$_{fl}$ (10 µM) in a buffer containing 20 mM Hepes
576 (pH 8.0), 50 mM KCl, 2 mM $MgCl_2$, 1 mM DTT, and 2 mM NaN_3. Samples were centrifuged at 100,000
577 g for 1 hr at 4°C. The supernatant and pellet were subjected to 4-15% gradient SDS-PAGE, followed by
578 Coomassie Brilliant Blue staining.

579 **Bioinformatics**

580 Multiple sequence alignments were generated using Clustal Omega[63]. The protein interaction
581 interfaces from the asymmetric unit were examined in detail using the PDBePISA server (Proteins,
582 Interfaces, Structures, and Assemblies)[64]. The DALI server was used for structural comparison[65].

583 **Data availability**

584 The plasmids generated in this study are available from the corresponding author upon request.
585 Protein coordinates and structure factors have been submitted to the Protein Data Bank under
586 accession codes.

587 PDB: 9G0C (bMERB$_{V978A_V985A}$:Rab10)

588 PDB: 9G0D (bMERB$_{V978A}$:Rab10)

589 Source data are provided with this paper.

590 ## References

591 1. Blanchoin, L., Boujemaa-Paterski, R., Sykes, C. & Plastino, J. Actin dynamics, architecture, and
592 mechanics in cell motility. *Physiol Rev* **94**, 235-63 (2014).
593 2. Pollard, T.D. Actin and Actin-Binding Proteins. *Cold Spring Harb Perspect Biol* **8**(2016).
594 3. Lappalainen, P., Kotila, T., Jegou, A. & Romet-Lemonne, G. Biochemical and mechanical
595 regulation of actin dynamics. *Nat Rev Mol Cell Biol* **23**, 836-852 (2022).
596 4. Varland, S., Vandekerckhove, J. & Drazic, A. Actin Post-translational Modifications: The
597 Cinderella of Cytoskeletal Control. *Trends Biochem Sci* **44**, 502-516 (2019).
598 5. Terman, J.R., Mao, T., Pasterkamp, R.J., Yu, H.H. & Kolodkin, A.L. MICALs, a family of conserved
599 flavoprotein oxidoreductases, function in plexin-mediated axonal repulsion. *Cell* **109**, 887-900
600 (2002).
601 6. Hung, R.J., Pak, C.W. & Terman, J.R. Direct redox regulation of F-actin assembly and
602 disassembly by Mical. *Science* **334**, 1710-3 (2011).
603 7. Hung, R.J., Spaeth, C.S., Yesilyurt, H.G. & Terman, J.R. SelR reverses Mical-mediated oxidation
604 of actin to regulate F-actin dynamics. *Nat Cell Biol* **15**, 1445-54 (2013).
605 8. Lee, B.C. et al. MsrB1 and MICALs regulate actin assembly and macrophage function via
606 reversible stereoselective methionine oxidation. *Mol Cell* **51**, 397-404 (2013).
607 9. Rajan, S., Terman, J.R. & Reisler, E. MICAL-mediated oxidation of actin and its effects on
608 cytoskeletal and cellular dynamics. *Front Cell Dev Biol* **11**, 1124202 (2023).
609 10. Cai, K. et al. MICAL1 facilitates pancreatic cancer proliferation, migration, and invasion by
610 activating WNT/beta-catenin pathway. *J Transl Med* **20**, 528 (2022).
611 11. Deng, W. et al. MICAL1 controls cell invasive phenotype via regulating oxidative stress in
612 breast cancer cells. *BMC Cancer* **16**, 489 (2016).
613 12. Zhao, S. et al. NEDD9 Facilitates Hypoxia-Induced Gastric Cancer Cell Migration via MICAL1
614 Related Rac1 Activation. *Front Pharmacol* **10**, 291 (2019).
615 13. Gu, H. et al. MICAL1 inhibits colorectal cancer cell migration and proliferation by regulating
616 the EGR1/beta-catenin signaling pathway. *Biochem Pharmacol* **195**, 114870 (2022).
617 14. Loria, R. et al. Sema6A and Mical1 control cell growth and survival of BRAFV600E human
618 melanoma cells. *Oncotarget* **6**, 2779-93 (2015).
619 15. Prifti, E. et al. Mical modulates Tau toxicity via cysteine oxidation in vivo. *Acta Neuropathol*
620 *Commun* **10**, 44 (2022).
621 16. Xu, C. et al. MICAL1 (molecule interacting with CasL 1) protects oligodendrocyte cells from
622 oxidative injury through regulating apoptosis, autophagy in spinal cord injury. *Neurosci Lett*
623 **750**, 135712 (2021).
624 17. Dazzo, E. et al. Mutations in MICAL-1cause autosomal-dominant lateral temporal epilepsy.
625 *Ann Neurol* **83**, 483-493 (2018).
626 18. Alto, L.T. & Terman, J.R. MICALs. *Curr Biol* **28**, R538-R541 (2018).
627 19. Suzuki, T. et al. MICAL, a novel CasL interacting molecule, associates with vimentin. *J Biol Chem*
628 **277**, 14933-41 (2002).
629 20. Van Battum, E.Y. et al. The intracellular redox protein MICAL-1 regulates the development of
630 hippocampal mossy fibre connections. *Nat Commun* **5**, 4317 (2014).
631 21. Fremont, S., Romet-Lemonne, G., Houdusse, A. & Echard, A. Emerging roles of MICAL family
632 proteins - from actin oxidation to membrane trafficking during cytokinesis. *J Cell Sci* **130**, 1509-
633 1517 (2017).

634 22. Stenmark, H. Rab GTPases as coordinators of vesicle traffic. *Nat Rev Mol Cell Biol* **10**, 513-25
635 (2009).
636 23. Barr, F. & Lambright, D.G. Rab GEFs and GAPs. *Curr Opin Cell Biol* **22**, 461-70 (2010).
637 24. Muller, M.P. & Goody, R.S. Molecular control of Rab activity by GEFs, GAPs and GDI. *Small*
638 *GTPases* **9**, 5-21 (2018).
639 25. Lamber, E.P., Siedenburg, A.C. & Barr, F.A. Rab regulation by GEFs and GAPs during membrane
640 traffic. *Curr Opin Cell Biol* **59**, 34-39 (2019).
641 26. Fremont, S. et al. Oxidation of F-actin controls the terminal steps of cytokinesis. *Nat Commun*
642 **8**, 14528 (2017).
643 27. Esposito, A. et al. Human MICAL1: Activation by the small GTPase Rab8 and small-angle X-ray
644 scattering studies on the oligomerization state of MICAL1 and its complex with Rab8. *Protein*
645 *Sci* **28**, 150-166 (2019).
646 28. Rai, A. et al. bMERB domains are bivalent Rab8 family effectors evolved by gene duplication.
647 *Elife* **5**(2016).
648 29. Rai, A., Goody, R.S. & Muller, M.P. Multivalency in Rab effector interactions. *Small GTPases*
649 **10**, 40-46 (2019).
650 30. Rai, A., Bleimling, N., Vetter, I.R. & Goody, R.S. The mechanism of activation of the actin
651 binding protein EHBP1 by Rab8 family members. *Nat Commun* **11**, 4187 (2020).
652 31. Jumper, J. et al. Highly accurate protein structure prediction with AlphaFold. *Nature* **596**, 583-
653 589 (2021).
654 32. Abou-Zeid, N. et al. MICAL-like1 mediates epidermal growth factor receptor endocytosis. *Mol*
655 *Biol Cell* **22**, 3431-41 (2011).
656 33. Sakane, A. et al. Rab13 small G protein and junctional Rab13-binding protein (JRAB)
657 orchestrate actin cytoskeletal organization during epithelial junctional development. *J Biol*
658 *Chem* **287**, 42455-68 (2012).
659 34. Miyake, K. et al. Actin Cytoskeletal Reorganization Function of JRAB/MICAL-L2 Is Fine-tuned
660 by Intramolecular Interaction between First LIM Zinc Finger and C-terminal Coiled-coil
661 Domains. *Sci Rep* **9**, 12794 (2019).
662 35. Sakane, A. et al. Conformational plasticity of JRAB/MICAL-L2 provides "law and order" in
663 collective cell migration. *Mol Biol Cell* **27**, 3095-3108 (2016).
664 36. Schmidt, E.F., Shim, S.O. & Strittmatter, S.M. Release of MICAL autoinhibition by semaphorin-
665 plexin signaling promotes interaction with collapsin response mediator protein. *J Neurosci* **28**,
666 2287-97 (2008).
667 37. Giridharan, S.S. & Caplan, S. MICAL-family proteins: Complex regulators of the actin
668 cytoskeleton. *Antioxid Redox Signal* **20**, 2059-73 (2014).
669 38. Zhang, N., Yao, L.L. & Li, X.D. Regulation of class V myosin. *Cell Mol Life Sci* **75**, 261-273 (2018).
670 39. Kelley, C.F. et al. Phosphoinositides regulate force-independent interactions between talin,
671 vinculin, and actin. *Elife* **9**(2020).
672 40. Siebold, C. et al. High-resolution structure of the catalytic region of MICAL (molecule
673 interacting with CasL), a multidomain flavoenzyme-signaling molecule. *Proc Natl Acad Sci U S*
674 *A* **102**, 16836-41 (2005).
675 41. Sun, H. et al. Solution structure of calponin homology domain of Human MICAL-1. *J Biomol*
676 *NMR* **36**, 295-300 (2006).
677 42. Sato, M. et al. Solution structures of the LIM domain of human NEDD9 interacting protein with
678 calponin homology and LIM domains. (RIKEN Structural Genomics/Proteomics Initiative
679 (RSGI), 2005).
680 43. McGarry, D.J. et al. MICAL1 activation by PAK1 mediates actin filament disassembly. *Cell Rep*
681 **41**, 111442 (2022).
682 44. Manta, B. & Gladyshev, V.N. Regulated methionine oxidation by monooxygenases. *Free Radic*
683 *Biol Med* **109**, 141-155 (2017).

684 45. Wu, H., Yesilyurt, H.G., Yoon, J. & Terman, J.R. The MICALs are a Family of F-actin Dismantling
685 Oxidoreductases Conserved from Drosophila to Humans. *Sci Rep* **8**, 937 (2018).
686 46. Zucchini, D., Caprini, G., Pasterkamp, R.J., Tedeschi, G. & Vanoni, M.A. Kinetic and
687 spectroscopic characterization of the putative monooxygenase domain of human MICAL-1.
688 *Arch Biochem Biophys* **515**, 1-13 (2011).
689 47. Oztug Durer, Z.A., Diraviyam, K., Sept, D., Kudryashov, D.S. & Reisler, E. F-actin structure
690 destabilization and DNase I binding loop: fluctuations mutational cross-linking and electron
691 microscopy analysis of loop states and effects on F-actin. *J Mol Biol* **395**, 544-57 (2010).
692 48. Das, S. et al. D-loop Dynamics and Near-Atomic-Resolution Cryo-EM Structure of Phalloidin-
693 Bound F-Actin. *Structure* **28**, 586-593 e3 (2020).
694 49. Grintsevich, E.E. et al. Catastrophic disassembly of actin filaments via Mical-mediated
695 oxidation. *Nat Commun* **8**, 2183 (2017).
696 50. Kobayashi, H., Etoh, K., Ohbayashi, N. & Fukuda, M. Rab35 promotes the recruitment of Rab8,
697 Rab13 and Rab36 to recycling endosomes through MICAL-L1 during neurite outgrowth. *Biol*
698 *Open* **3**, 803-14 (2014).
699 51. Sun, Y., Bilan, P.J., Liu, Z. & Klip, A. Rab8A and Rab13 are activated by insulin and regulate
700 GLUT4 translocation in muscle cells. *Proc Natl Acad Sci U S A* **107**, 19909-14 (2010).
701 52. Vitali, T., Maffioli, E., Tedeschi, G. & Vanoni, M.A. Properties and catalytic activities of MICAL1,
702 the flavoenzyme involved in cytoskeleton dynamics, and modulation by its CH, LIM and C-
703 terminal domains. *Arch Biochem Biophys* **593**, 24-37 (2016).
704 53. Koch, D. et al. A pull-down procedure for the identification of unknown GEFs for small
705 GTPases. *Small GTPases* **7**, 93-106 (2016).
706 54. Pan, D., Brockmeyer, A., Mueller, F., Musacchio, A. & Bange, T. Simplified Protocol for Cross-
707 linking Mass Spectrometry Using the MS-Cleavable Cross-linker DSBU with Efficient Cross-link
708 Identification. *Anal Chem* **90**, 10990-10999 (2018).
709 55. Chambers, M.C. et al. A cross-platform toolkit for mass spectrometry and proteomics. *Nat*
710 *Biotechnol* **30**, 918-20 (2012).
711 56. Arlt, C. et al. Integrated Workflow for Structural Proteomics Studies Based on Cross-
712 Linking/Mass Spectrometry with an MS/MS Cleavable Cross-Linker. *Anal Chem* **88**, 7930-7
713 (2016).
714 57. Gotze, M. et al. Automated assignment of MS/MS cleavable cross-links in protein 3D-structure
715 analysis. *J Am Soc Mass Spectrom* **26**, 83-97 (2015).
716 58. Graham, M., Combe, C., Kolbowski, L. & Rappsilber, J. xiView: A common platform for the
717 downstream analysis of Crosslinking Mass Spectrometry data. *bioRxiv* (2019).
718 59. Kabsch, W. Xds. *Acta Crystallogr D Biol Crystallogr* **66**, 125-32 (2010).
719 60. McCoy, A.J. et al. Phaser crystallographic software. *J Appl Crystallogr* **40**, 658-674 (2007).
720 61. Emsley, P., Lohkamp, B., Scott, W.G. & Cowtan, K. Features and development of Coot. *Acta*
721 *Crystallogr D Biol Crystallogr* **66**, 486-501 (2010).
722 62. Adams, P.D. et al. PHENIX: a comprehensive Python-based system for macromolecular
723 structure solution. *Acta Crystallogr D Biol Crystallogr* **66**, 213-21 (2010).
724 63. Sievers, F. et al. Fast, scalable generation of high-quality protein multiple sequence alignments
725 using Clustal Omega. *Mol Syst Biol* **7**, 539 (2011).
726 64. Krissinel, E. & Henrick, K. Inference of macromolecular assemblies from crystalline state. *J Mol*
727 *Biol* **372**, 774-97 (2007).
728 65. Holm, L. Benchmarking fold detection by DaliLite v.5. *Bioinformatics* **35**, 5326-5327 (2019).

729

Acknowledgments

We are grateful to Prof. Maria Vanoni for sharing the full-length Mical1, MO-CH-LIM, MO-CH, and MO bacterial expression constructs and providing the purification protocol. We also thank the beamline staff of the Swiss Light Source (SLS) X10SA at the Paul Scherrer Institute, Villigen, Switzerland, and the beamline staff of the European Synchrotron Radiation Facility at Grenoble, France, for their assistance during data collection. We thank Dr. Raphael Gasper and Dr. Matthias Müller for the X-ray diffraction data collection. We express our gratitude to Petra Geue for conducting the SEC-MALS measurements and data analysis. Special thanks are extended to Franziska Müller for her contributions to the size exclusion chromatography experiment for the peptides. We are thankful to Malte Metz and Andreas Brockmeyer for conducting the LC-MS/MS runs and method setup. Additionally, we acknowledge financial support from the Max-Planck-Society and the Deutsche Forschungsgemeinschaft (grant GO 284/10-1 to R.S.G). Open access funding provided by Max Planck Society.

Author contributions

A.R. conceived and designed the study, carried out protein expression and purification, conducted all biochemical studies, cross-linking experiments, crystallization, and determined X-ray structures. P.J. performed LC-MS/MS experiments, conducted data analysis, and identified cross-links. I.R.V. conducted Mical1 AlphaFold2 modeling and analyzed the structure. R.S.G. acquired funding. A.R., P.J., I.R.V., and R.S.G. analyzed and interpreted the data. A.R. wrote the manuscript with critical input from all authors.

Competing interests

The authors declare no competing interest.

Figure Legends

Fig. 1: Mical1 MO-CH-LIM domains form an intramolecular complex with its bMERB domain. (a) A schematic diagram of human Mical1: Mical1 contains an N-terminal monooxygenase (MO) domain, calponin homology (CH) domain, Lin11, Isl-1, and Mec-3 (LIM) domain, and a C-terminal coiled-coil bMERB (bivalent Mical/EHBP Rab binding) domain. PRM: proline-rich motif. (**b-f**) Size exclusion chromatography (Superdex 200) coupled with multi-angle light scattering (SEC-MALS) was performed for full-length Mical1, MO-CH-LIM, MO-CH, and MO, while size exclusion chromatography (Superdex 75) coupled with SEC-MALS was conducted for the bMERB domain. The Rayleigh scattering is represented in blue, and the molecular weight distribution across the peak is shown in gray. The

760 measured molecular weight closely corresponds to that of a monomer. (**g-i)** MO-CH-LIM domain
761 construct interacts with the bMERB domain. Binding affinities were measured by titrating the bMERB
762 domain (600 µM) with the MO-CH-LIM/MO-CH/MO domain (40 µM). Integrated heat peaks, corrected
763 for the offset by subtracting the control experiment, were fitted to a one-site-binding model, yielding
764 the binding stoichiometry (N), enthalpy (ΔH), entropy (ΔS), and dissociation constant (K_D). Clear
765 complex formation was observed for the MO-CH-LIM, whereas no complex formation was observed
766 for the MO-CH and MO. The data represents results from at least three independent experiments.
767 N.D. denotes not detected.

768 **Fig. 2: Full-length bMERB domain is essential for interaction with MO-CH-LIM domains. (a-c)** The full-
769 length bMERB domain is required for MO-CH-LIM interaction. Binding affinities were measured by
770 titrating the bMERB/$bMERB_{H1-2}$/$bMERB_{H2-3}$ domain (600 µM) with the MO-CH-LIM domain (40 µM).
771 Integrated heat peaks, corrected for the offset by subtracting the control experiment, were fitted to
772 a one-site-binding model, yielding the binding stoichiometry (N), enthalpy (ΔH), entropy (ΔS), and
773 dissociation constant (K_D). The data clearly show that the full-length bMERB construct is necessary for
774 interaction with MO-CH-LIM. The data are representative of at least three repetitions. N.D. denotes
775 not detected. (**d)** The Coomassie blue-stained SDS-PAGE analysis of purified Mical1 and the MO-CH-
776 LIM:bMERB complex proteins, incubated in the absence or presence of the crosslinker disuccinimidyl
777 dibutyric urea (DSBU), demonstrates efficient DSBU-dependent crosslinking. (**e-f)** Intramolecular
778 crosslinking of Mical1. (**e)** Schematic visualization showing inter- and intra-domain crosslinks identified
779 by mass spectrometry analysis of purified full-length Mical1 crosslinked by DSBU. Crosslinks are shown
780 in light purple. (**f**) Schematic diagram showing inter and intra-domain crosslinks between purified MO-
781 CH-LIM and bMERB domain crosslinked by DSBU. Schematic diagram illustrating inter- and intra-
782 domain crosslinks between the purified MO-CH-LIM and bMERB domains, crosslinked by DSBU. Self-
783 crosslinks are shown in light purple, whereas crosslinks between the isolated MO-CH-LIM and bMERB
784 domains are shown in light blue.

785 **Fig. 3: AlphaFold2 model of auto-inhibited Mical1. (a)** The cartoon representation of the AlphaFold2
786 Mical1 model. The MO domain, CH domain, LIM domain, the helix connecting the CH and LIM domains
787 ($Helix^{CHL}$), and the bMERB domain of Mical1 are colored in orange, pink, blue, gray, and green,
788 respectively. The insets highlight the various binding interfaces between the MO:bMERB, CH:bMERB,
789 LIM:bMERB, and $Helix^{CHL}$:bMERB domains, with hydrogen bonds and salt bridges indicated by gray
790 dashed lines. (**b-c)** The cartoon representation of the bMERB domain depicts the MO domain, CH
791 domain, LIM domain, and $Helix^{CHL}$ binding interfaces in orange, pink, blue, and gray dashed lines,
792 respectively. The hydrophobic patches are shown in red dashed lines on the bMERB domain. (**d)**
793 Structural alignment was performed between the oxidized mouse Mical1 MO domain (light orange,

794 PDB: 2BRY) and the reduced mouse Mical1 MO domain (slate, PDB: 2C4C), and both were compared
795 with the human Mical1 AlphaFold2 model (MO domain in orange and bMERB domain in green). **(e)**
796 Schematic illustration showing the movement of the isoalloxazine ring of the FAD head during the
797 catalytic cycle upon NADPH treatment. Insets depict the conformational changes of several active site
798 residues upon NADPH treatment. (**f)** Results from a systematic analysis of the binding interfaces
799 between various domains of the AlphaFold2-predicted Mical1 auto-inhibited model using PISA[64].

800 **Fig. 4: Crucial bMERB interface residues for MO-CH-LIM interaction. (a)** Schematic illustration of the
801 interactions between the MO-CH-LIM and the bMERB domain. Hydrophobic interactions are
802 represented by light orange dashed lines, while hydrogen bonds (H-bonds) and salt bridges are
803 depicted with gray dashed lines. Residues that have been mutated are highlighted in red dashed
804 boxes. (**b–i)** Mutational alanine screening of the bMERB domain via ITC measurements. The binding
805 of different bMERB mutants (600 µM) with MO-CH-LIM (40 µM) was systematically tested and
806 affinities were determined by ITC experiments. Integrated heat peaks, corrected for the offset by
807 subtracting the control experiment, were fitted to a one-site-binding model, yielding the binding
808 stoichiometry (N), enthalpy (ΔH), entropy (ΔS), and dissociation constant (K_D). N.D. denotes not
809 detected. No binding was detected for the mutant F925A or the mutant L1047A_F1050A. However, a
810 more than 5-fold reduction in binding affinity was observed for all other mutants, except for
811 K918A_E921A, which exhibited a marginal defect. The data represent at least three repetitions.

812 **Fig. 5: Allostery between the Rab binding domains. (a)** A schematic diagram of human Mical1. **(b)** Full
813 length Mical1 binds to Rab8 in 1:2 stoichiometry. Binding affinities were measured by titrating the
814 Rab8 (800 µM) to full-length Mical1 (40 µM). Integrated heat peaks were fitted to a two-site-binding
815 model yielding the binding stoichiometry (N), the enthalpy (ΔH), the entropy (ΔS), and the dissociation
816 constant (K_D). **(c)** Cartoon representation of the bMERB:Rab10 complex structure (PDB: 5LPN)[28], with
817 the bMERB domain colored in green and the Rab10 domain in wheat. **(c-d)** Schematic illustration of
818 the interactions between the bMERB domain and Rab10. Rab10 binds to the Mical1 bMERB domain
819 via its N-terminal regions, switch regions, and inter-switch region. Hydrogen bonds and salt bridges
820 are depicted with gray dashed lines, while light orange dashed lines indicate hydrophobic interactions.
821 RabSF1, RabSF2, RabF1, RabF2, RabF3, and RabF4 motifs are colored in orange, gray, green, pink,
822 purple, and brown, respectively. Additionally, analytical size exclusion chromatography results are
823 provided from a systematic analysis of interactions between the bMERB domain mutants and
824 increasing concentrations of Rab8 (refer to Supplementary Fig. 4 and 5). (**e-g, m-n)** The bMERB domain
825 (green), Rab8 (gray), and a mixture of both (blue) were loaded onto a Superdex 75 10/300 GL column
826 to monitor for complex formation. (**h-l, o-p)** Binding affinities were measured by titrating the Rab8
827 (600 µM) to mutants bMERB domain (30 µM). Integrated heat peaks were fitted to a one-site-binding

828 or two-site-binding model yielding the binding stoichiometry (N), the enthalpy (ΔH), the entropy (ΔS),
829 and the dissociation constant (K_D). The data are representative of at least three repetitions.

830 **Fig. 6: Crystal structure of the bMERB$_{V978A_V985A}$:Rab10 complex. (a)** Cartoon depiction of the
831 bMERB$_{V978A_V985A}$:Rab10 complex. A single Rab10 molecule (gray) binds to the bMERB$_{V978A_V985A}$ domain
832 (blue) at the high-affinity C-terminal Rab-binding site. Switch I and Switch II of Rab10 are shown in red
833 and blue, respectively. GppNHp and Mg^{2+} are depicted as sticks and a green sphere, respectively. **(b)**
834 Structural superposition of the bMERB$_{V978A_V985A}$:Rab10 complex and bMERB:Rab10 complex (PDB:
835 5LPN)[28]. **(c)** Structural alignment of the bMERB domains of bMERB$_{V978A_V985A}$:Rab10 (blue) with the
836 bMERB:Rab10 (PDB: 5LPN)[28] and the bMERB domain (PDB: 5LEO)[26].

837 **Fig. 7: Phosphomimetic mutation of bMERB S960D does not affect Rab8 family member binding. (a)**
838 The schematic diagram of human Mical1 shows an N-terminal monooxygenase (MO) domain, a
839 calponin homology (CH) domain, a Lin11, Isl-1, and Mec-3 (LIM) domain, and a C-terminal coiled-coil
840 bMERB (bivalent Mical/EHBP Rab binding) domain, along with PAK1 phosphorylation sites S817 and
841 S960. **(b)** The surface electrostatic potential of bMERB was calculated in PyMOL using the APBS-
842 PDB2PQR plugin and visualized with colors ranging from red (-5 kT/e) to blue (+5 kT/e). AlphaFold2
843 predicted the Mical1 amino acids 807–820, with S817 shown in stick representation. The side chain of
844 S817 points towards a negatively charged patch on the Mical1 bMERB domain. **(c)** Cartoon
845 representation of the Mical1 bMERB domain (PDB: 5LPN)[28], with S960 shown in stick representation.
846 Rab10 binding sites are indicated with dashed circles. **(d, e, h-k)** Binding of Rab8a (gray)/Rab10
847 (wheat)/Rab15 (red) with different Mical1 bMERB domain (green) was systematically tested onto a
848 Superdex 75 10/300 GL column. **(f, g, l-o)** Binding affinities were measured by ITC experiments. Binding
849 affinities were measured by titrating the Rab8/Rab10/Rab15 (600 µM) to wild type/mutant bMERB
850 domain (30 µM). Integrated heat peaks were fitted to a two-site-binding model yielding the binding
851 stoichiometry (N), the enthalpy (ΔH), the entropy (ΔS), and the dissociation constant (K_D).
852 Phosphomimetic mutation of S960 of the bMERB domain does not affect interaction with
853 Rab8/Rab10/Rab15. The data are representative of at least three repetitions.

854 **Fig. 8: Impact of Rab binding site mutations in the bMERB domain on MO-CH-LIM interaction. (a)**
855 Schematic illustration of the interactions between the MO-CH-LIM domain and the bMERB domain.
856 Hydrophobic interactions are indicated by light orange dashed lines, and hydrogen bonds are
857 indicated by gray dashed lines. **(b-i)** Effect of RBS mutants on MO-CH-LIM:bMERB domain interaction.
858 The binding of MO-CH-LIM with different RBS bMERB mutants was systematically tested, and affinities
859 were determined by ITC experiments. Integrated heat peaks, corrected for the offset by subtracting
860 the control experiment, were fitted to a one-site-binding model, yielding the binding stoichiometry

861 (N), enthalpy (ΔH), entropy (ΔS), and dissociation constant (K_D). N.D. denotes not detected. The data
862 are representative of at least three repetitions.

863 **Fig. 9: Structural basis of Mical1 activation upon Rab8 binding. (a)** Structural superposition of the
864 Mical1 auto-inhibited AlphaFold2 model and the bMERB:Rab10 complex (PDB: 5LPN)[28]. (**b)** Structural
865 overlay clearly shows that the binding of the first Rab molecule at high affinity stabilizes the helix 3
866 conformation, which structurally interferes with the CH domain and $Helix^{CHL}$ binding site. Additionally,
867 the movement of helices 1-2 strictly hinders the CH binding site. **(c)** The superimposition of the bMERB
868 domain of Mical1 in the auto-inhibited AlphaFold2 model with the bMERB domain of the
869 bMERB:Rab10 complex (PDB: 5LPN)[28] reveals the movement of bMERB helices upon Rab binding. **(d)**
870 Structural overlay of the bMERB domain of Mical1 in the auto-inhibited state Alphafold2 model with
871 the bMERB domain of the bMERB:Rab10 complex (PDB: 5LPN)[28], with an inset highlighting the
872 conformational changes of interface residues upon Rab10 binding. **(e)** The results of systematic
873 analysis of interactions between full-length Mical1 or different Mical1 deletion constructs with F-actin
874 via co-sedimentation experiments reveal that the MO domain is the minimal domain required for
875 interaction with F-actin, whereas the full-length Mical1 exhibits perturbed interaction with F-actin.
876 These experiments were independently repeated at least three times with consistent results.

877 **Fig. 10: The activation mechanism of Mical1 by Rab8 family members.** In the absence of active Rab8,
878 Mical1 exists in an auto-inhibited state, where the MO, CH, $Helix^{CHL}$, and LIM domains interact with its
879 bMERB domain. Rab8 is recruited to the membrane by its GEF molecule (e.g., Rabin 8 or GRAB). The
880 first molecule of active Rab8 binds to the high-affinity C-terminal binding site, leading to a change in
881 the conformation of helix 3, which displaces the CH domain and $Helix^{CHL}$. The first binding of the Rab
882 molecule also changes the conformation of helix 2 and helix 3 at the low-affinity N-terminal Rab
883 binding site, further interfering with CH binding, and this conformation leads to a change in the LIM
884 and MO binding interface on the bMERB domain, resulting in the displacement of the LIM and MO
885 domains. The second Rab8 molecule binds to stabilize the active state of the enzyme, allowing the MO
886 domain to be available for F-actin interaction, leading to the depolymerization of F-actin.

Fig1

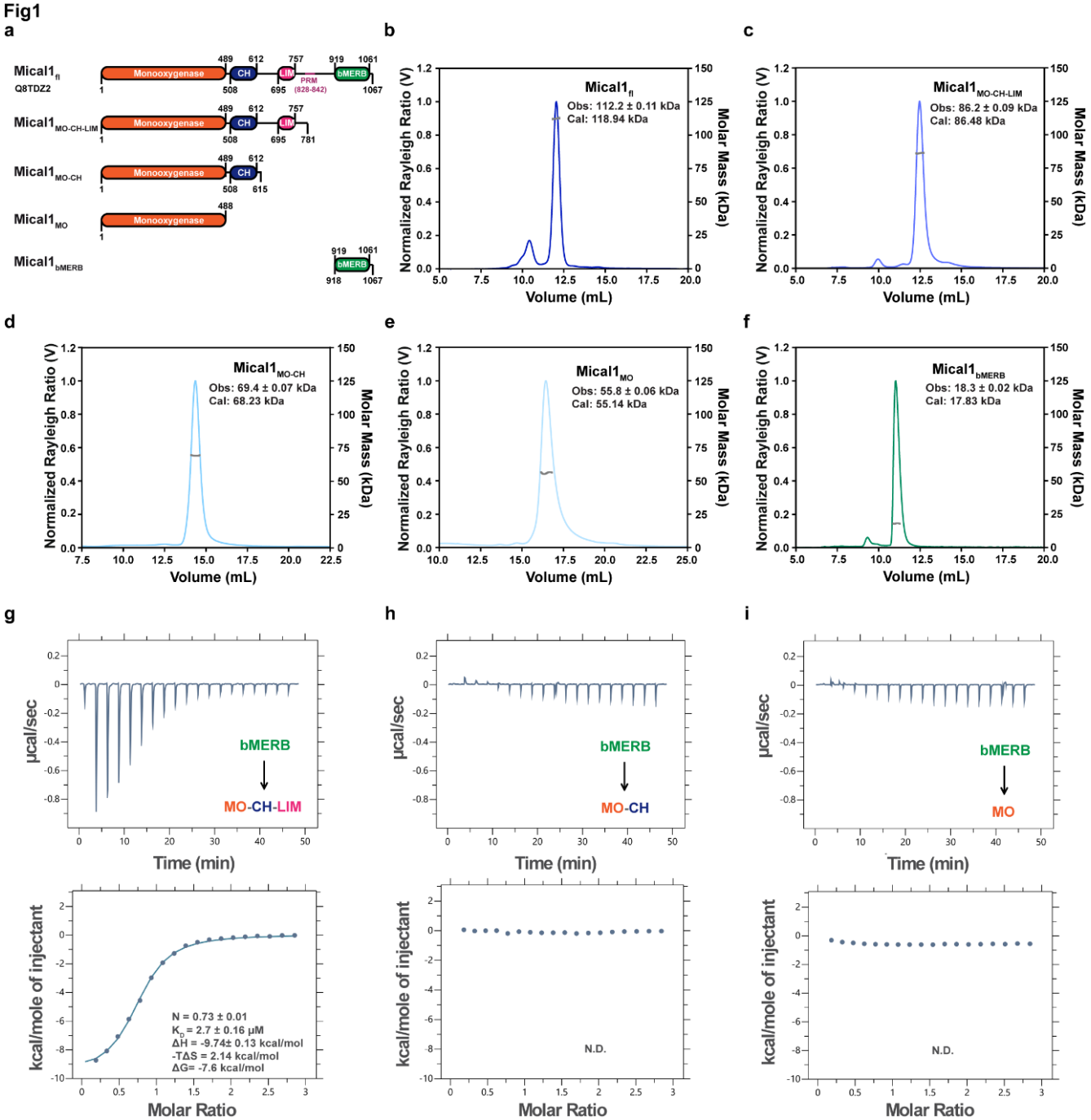
a
Mical1fl
Q8TDZ2
Monooxygenase
CH
LIM
PRM
(828-842)
bMERB
Mical1MO-CH-LIM
Mical1MO-CH
Mical1MO
Mical1bMERB
b
Mical1fl
Obs: 112.2 ± 0.11 kDa
Cal: 118.94 kDa
c
Mical1MO-CH-LIM
Obs: 86.2 ± 0.09 kDa
Cal: 86.48 kDa
d
Mical1MO-CH
Obs: 69.4 ± 0.07 kDa
Cal: 68.23 kDa
e
Mical1MO
Obs: 55.8 ± 0.06 kDa
Cal: 55.14 kDa
f
Mical1bMERB
Obs: 18.3 ± 0.02 kDa
Cal: 17.83 kDa
Normalized Rayleigh Ratio (V)
Molar Mass (kDa)
Volume (mL)
g
h
i
µcal/sec
Time (min)
bMERB
MO-CH-LIM
MO-CH
MO
kcal/mole of injectant
Molar Ratio
N = 0.73 ± 0.01
KD = 2.7 ± 0.16 µM
ΔH = -9.74± 0.13 kcal/mol
-TΔS = 2.14 kcal/mol
ΔG= -7.6 kcal/mol
N.D.

Fig2

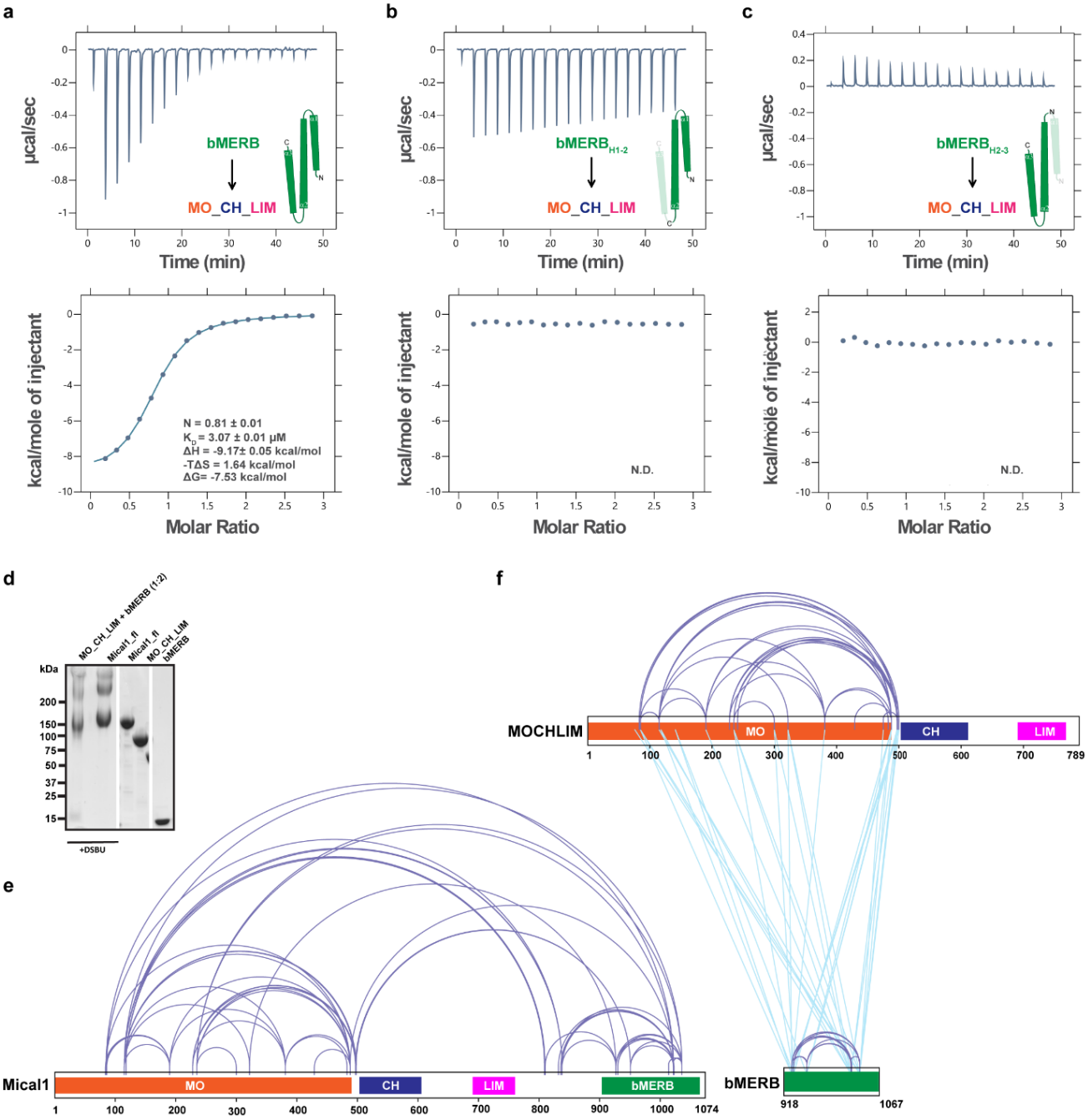
a
b
c
µcal/sec
Time (min)
bMERB
MO_CH_LIM
bMERB H1-2
bMERB H2-3
kcal/mole of injectant
Molar Ratio
N = 0.81 ± 0.01
K_D = 3.07 ± 0.01 µM
ΔH = -9.17± 0.05 kcal/mol
-TΔS = 1.64 kcal/mol
ΔG= -7.53 kcal/mol
N.D.
d
MO_CH_LIM + bMERB (1:2)
Mical1_fl
Mical1_fl
MO_CH_LIM
bMERB
kDa
+DSBU
e
Mical1
MO
CH
LIM
bMERB
f
MOCHLIM
bMERB

Fig3

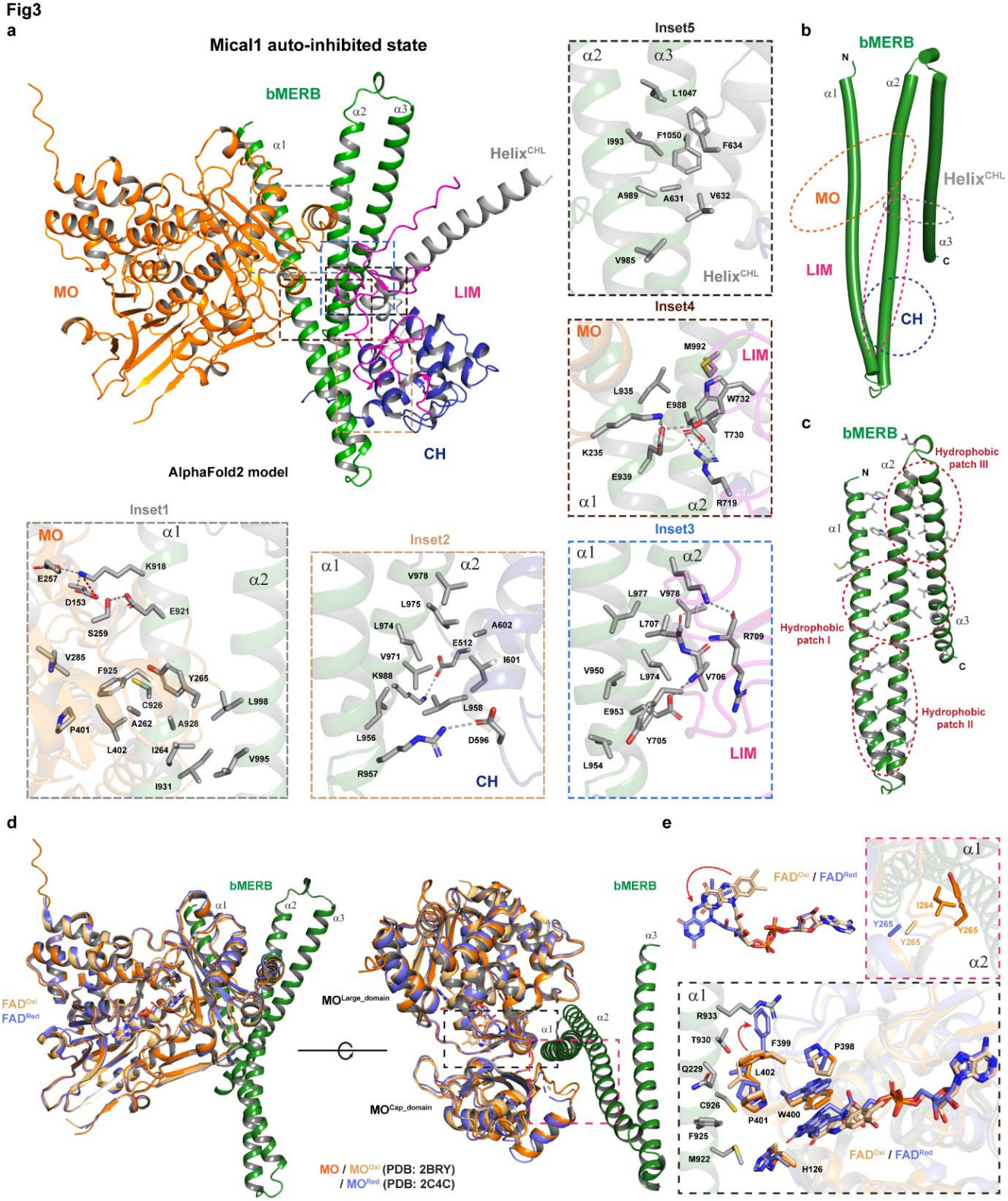

f

PISA	MO (1-488 aa)	CH (508-613 aa)	Helix^CHL (624-654 aa)	LIM (692-751 aa)	Linker (800-855 aa)	bMERB (886-1067 aa)
MO (1-488 aa)	—			310.9 Å²	381.2 Å²	1190 Å²
CH (508-613 aa)		—	297.8 Å²	309.6 Å²		506.5 Å²
Helix^CHL (624-654 aa)			—	255 Å²		462.6 Å²
LIM (692-751 aa)				—		652.4 Å²
Linker (800-855 aa)					—	158.1 Å²

Fig4

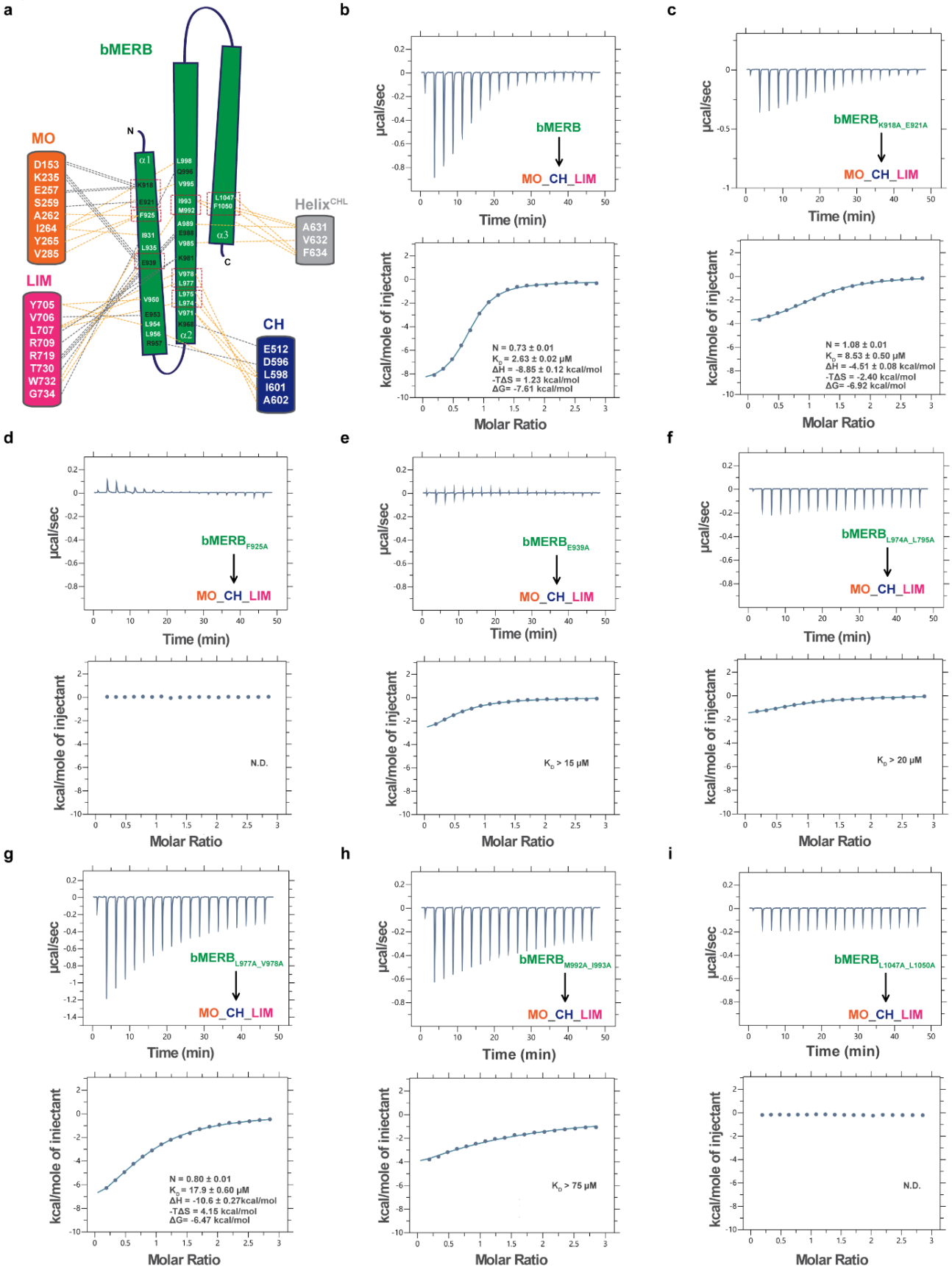
a
bMERB
MO
D153
K235
E257
S259
A262
I264
Y265
V285
LIM
Y705
V706
L707
R709
R719
T730
W732
G734
N
C
α1
α2
α3
K918
E921
F925
I931
L935
E939
V950
E953
L954
L956
R957
L998
Q996
V995
I993
M992
A989
L988
V985
K981
V978
L977
L976
L974
V971
K968
L1047
F1050
Helix^CHL
A631
V632
F634
CH
E512
D596
L598
I601
A602
b
bMERB
MO_CH_LIM
µcal/sec
Time (min)
kcal/mole of injectant
Molar Ratio
N = 0.73 ± 0.01
K_D = 2.63 ± 0.02 µM
ΔH = -8.85 ± 0.12 kcal/mol
-TΔS = 1.23 kcal/mol
ΔG= -7.61 kcal/mol
c
bMERB_K918A_E921A
MO_CH_LIM
N = 1.08 ± 0.01
K_D = 8.53 ± 0.50 µM
ΔH = -4.51 ± 0.08 kcal/mol
-TΔS = -2.40 kcal/mol
ΔG= -6.92 kcal/mol
d
bMERB_F925A
MO_CH_LIM
N.D.
e
bMERB_E939A
MO_CH_LIM
K_D > 15 µM
f
bMERB_L974A_L795A
MO_CH_LIM
K_D > 20 µM
g
bMERB_L977A_V978A
MO_CH_LIM
N = 0.80 ± 0.01
K_D = 17.9 ± 0.60 µM
ΔH = -10.6 ± 0.27kcal/mol
-TΔS = 4.15 kcal/mol
ΔG= -6.47 kcal/mol
h
bMERB_M992A_I993A
MO_CH_LIM
K_D > 75 µM
i
bMERB_L1047A_L1050A
MO_CH_LIM
N.D.

Fig5

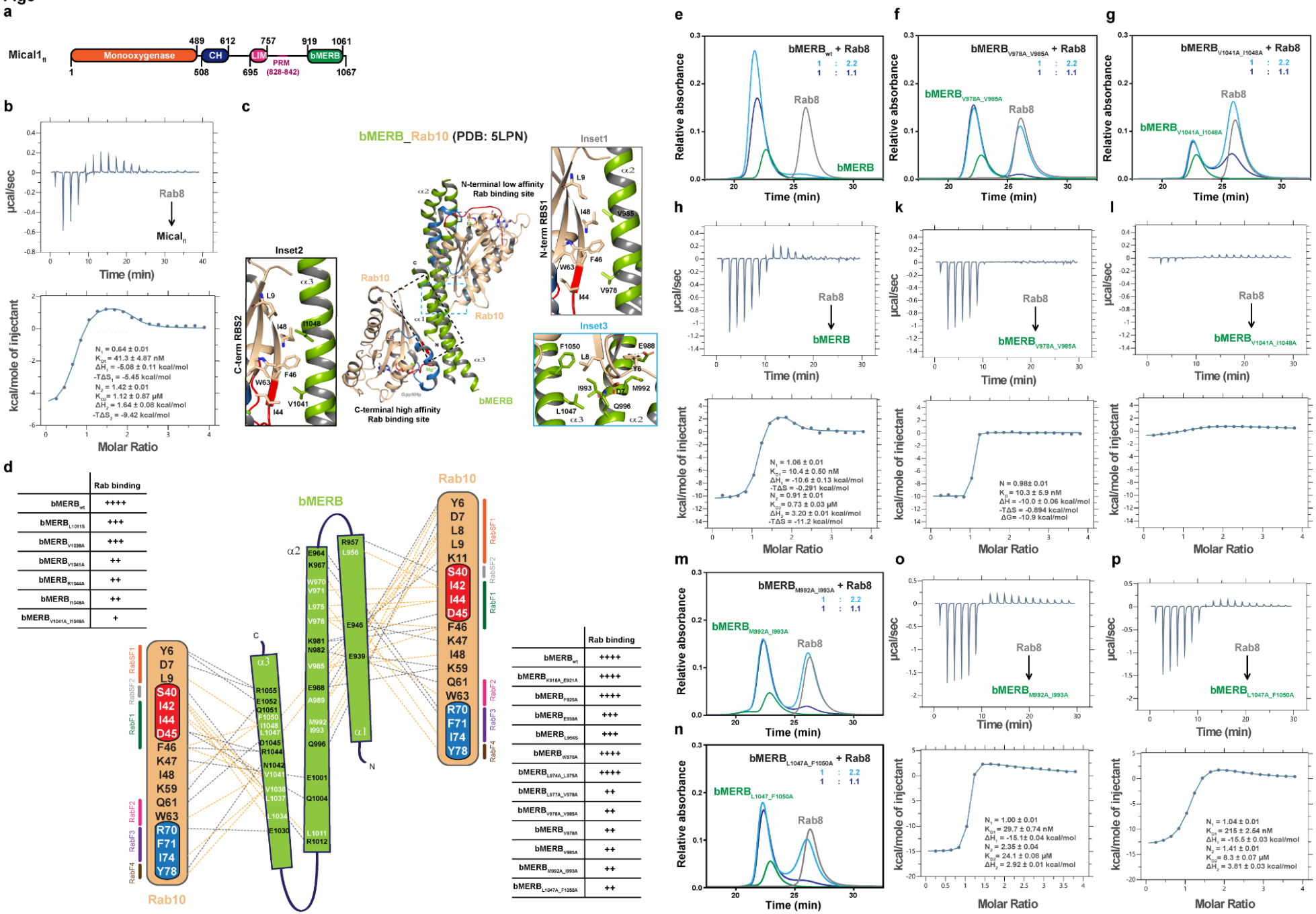
a
Mical1fl
Monooxygenase
CH
LIM
PRM (828-842)
bMERB
489 612 757 919 1061
1 508 695 1067
b
Rab8
Micalfl
Time (min)
kcal/mole of injectant
Molar Ratio
N1 = 0.64 ± 0.01
KD1 = 41.3 ± 4.87 nM
ΔH1 = -5.08 ± 0.11 kcal/mol
-TΔS1 = -5.45 kcal/mol
N2 = 1.42 ± 0.01
KD2 = 1.12 ± 0.87 μM
ΔH2 = 1.64 ± 0.08 kcal/mol
-TΔS2 = -9.42 kcal/mol
c
bMERB_Rab10 (PDB: 5LPN)
N-terminal low affinity Rab binding site
C-terminal high affinity Rab binding site
Rab10
bMERB
Inset1
Inset2
Inset3
N-term RBS1
C-term RBS2
d
Rab binding
bMERBwt ++++
bMERBL1011S +++
bMERBV1039A +++
bMERBV1041A ++
bMERBR1044A ++
bMERBI1048A ++
bMERBV1041A_I1048A +
Rab binding
bMERBwt ++++
bMERBK918A_E921A ++++
bMERBF925A ++++
bMERBE939A +++
bMERBL956S +++
bMERBW970A ++++
bMERBL974A_L975A ++++
bMERBL977A_V978A ++
bMERBV978A_V985A ++
bMERBV978A ++
bMERBV985A ++
bMERBM992A_I993A ++
bMERBL1047A_F1050A ++
e
bMERBwt + Rab8
1 : 2.2
1 : 1.1
Rab8
bMERB
Relative absorbance
Time (min)
f
bMERBV978A_V985A + Rab8
bMERBV978A_V985A
g
bMERBV1041A_I1048A + Rab8
bMERBV1041A_I1048A
h
k
l
N1 = 1.06 ± 0.01
KD1 = 10.4 ± 0.50 nM
ΔH1 = -10.6 ± 0.13 kcal/mol
-TΔS = -0.291 kcal/mol
N2 = 0.91 ± 0.01
KD2 = 0.73 ± 0.03 μM
ΔH2 = 3.20 ± 0.01 kcal/mol
-TΔS = -11.2 kcal/mol
N = 0.98± 0.01
KD = 10.3 ± 5.9 nM
ΔH = -10.0 ± 0.06 kcal/mol
-TΔS = -0.894 kcal/mol
ΔG= -10.9 kcal/mol
m
bMERBM992A_I993A + Rab8
bMERBM992A_I993A
o
p
bMERBL1047A_F1050A
n
bMERBL1047A_F1050A + Rab8
bMERBL1047_F1050A
N1 = 1.00 ± 0.01
KD1 = 29.7 ± 0.74 nM
ΔH1 = -15.1± 0.04 kcal/mol
N2 = 2.35 ± 0.04
KD2 = 24.1 ± 0.08 μM
ΔH2 = 2.92 ± 0.01 kcal/mol
N1 = 1.04 ± 0.01
KD1 = 215 ± 2.54 nM
ΔH1 = -15.5 ± 0.03 kcal/mol
N2 = 1.41 ± 0.01
KD2 = 8.3 ± 0.07 μM
ΔH2 = 3.81 ± 0.03 kcal/mol

Fig6

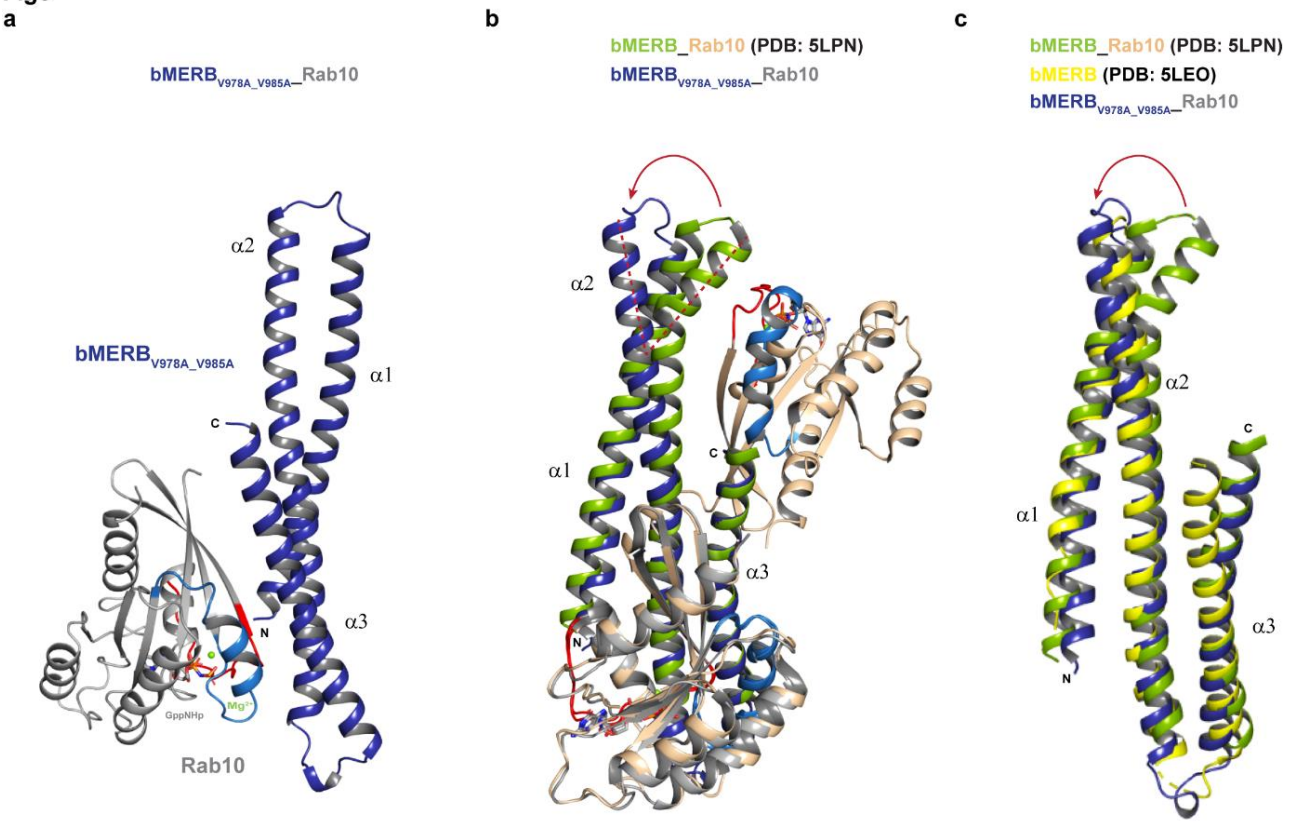
a
bMERB$_{V978A_V985A}$–Rab10
α2
bMERB$_{V978A_V985A}$
α1
C
N
α3
GppNHp
Mg^{2+}
Rab10
b
bMERB_Rab10 (PDB: 5LPN)
bMERB$_{V978A_V985A}$–Rab10
α2
α1
C
α3
N
c
bMERB_Rab10 (PDB: 5LPN)
bMERB (PDB: 5LEO)
bMERB$_{V978A_V985A}$–Rab10
α2
C
α1
α3
N

Fig7

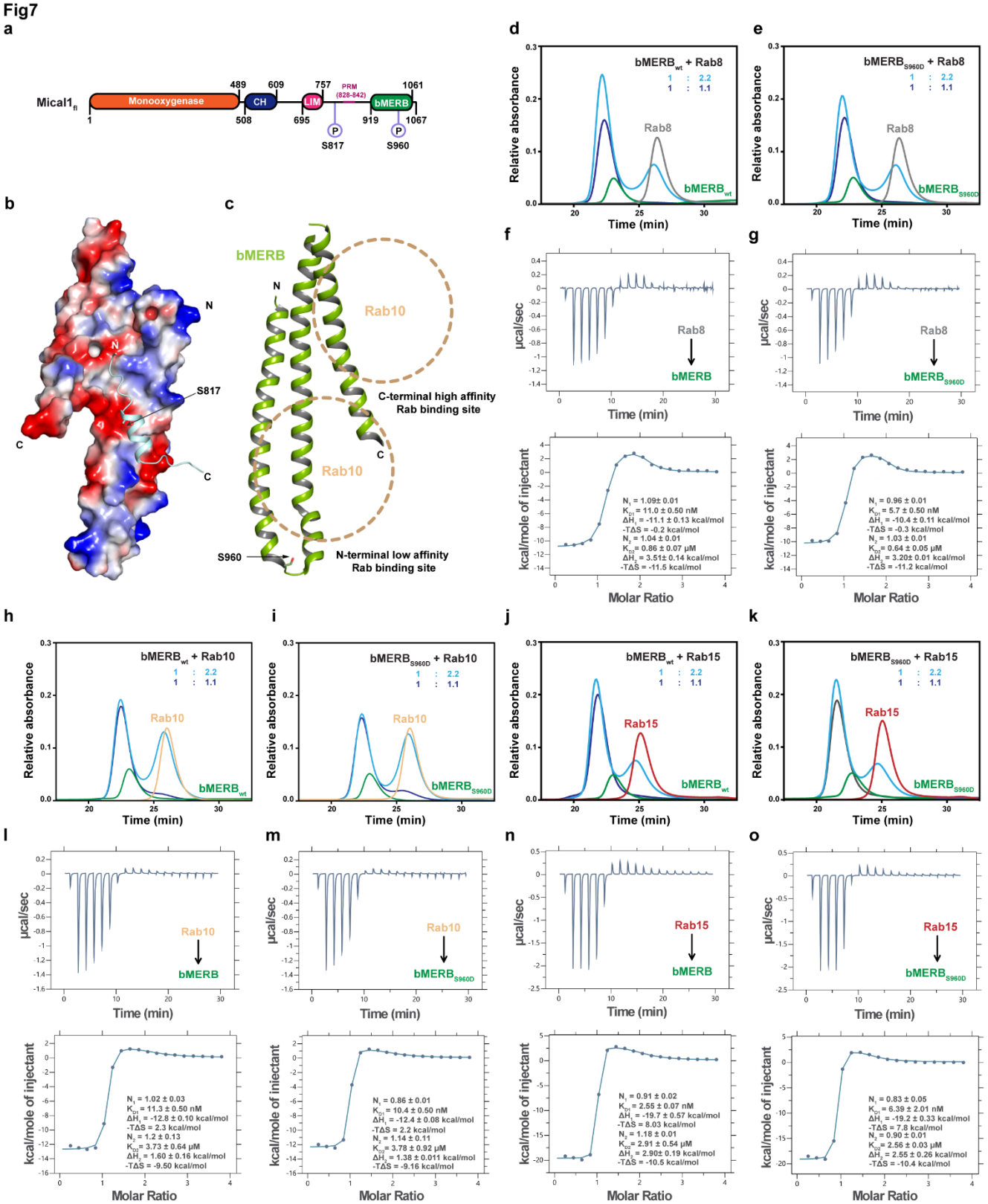
a
Mical1fl
Monooxygenase
CH
LIM
PRM (828-842)
bMERB
489
609
757
1061
1
508
695
919
1067
P
S817
S960
b
N
S817
C
c
bMERB
Rab10
C-terminal high affinity Rab binding site
N-terminal low affinity Rab binding site
d
bMERBwt + Rab8
1 : 2.2
1 : 1.1
Rab8
bMERBwt
Relative absorbance
Time (min)
e
bMERBS960D + Rab8
bMERBS960D
f
µcal/sec
Rab8
bMERB
kcal/mole of injectant
Molar Ratio
N1 = 1.09± 0.01
K21 = 11.0 ± 0.50 nM
ΔH1 = -11.1 ± 0.13 kcal/mol
-TΔS = -0.2 kcal/mol
N2 = 1.04 ± 0.01
K22 = 0.86 ± 0.07 µM
ΔH2 = 3.51± 0.14 kcal/mol
-TΔS = -11.5 kcal/mol
g
N1 = 0.96 ± 0.01
K21 = 5.7 ± 0.50 nM
ΔH1 = -10.4 ± 0.11 kcal/mol
-TΔS = -0.3 kcal/mol
N2 = 1.03 ± 0.01
K22 = 0.64 ± 0.05 µM
ΔH2 = 3.20± 0.01 kcal/mol
-TΔS = -11.2 kcal/mol
h
bMERBwt + Rab10
i
bMERBS960D + Rab10
j
bMERBwt + Rab15
Rab15
k
bMERBS960D + Rab15
l
N1 = 1.02 ± 0.03
K21 = 11.3 ± 0.50 nM
ΔH1 = -12.8 ± 0.10 kcal/mol
-TΔS = 2.3 kcal/mol
N2 = 1.2 ± 0.13
K22 = 3.73 ± 0.64 µM
ΔH2 = 1.60 ± 0.16 kcal/mol
-TΔS = -9.50 kcal/mol
m
N1 = 0.86 ± 0.01
K21 = 10.4 ± 0.50 nM
ΔH1 = -12.4 ± 0.08 kcal/mol
-TΔS = 2.2 kcal/mol
N2 = 1.14 ± 0.11
K22 = 3.78 ± 0.92 µM
ΔH2 = 1.38 ± 0.011 kcal/mol
-TΔS = -9.16 kcal/mol
n
N1 = 0.91 ± 0.02
K21 = 2.55 ± 0.07 nM
ΔH1 = -19.7 ± 0.57 kcal/mol
-TΔS = 8.03 kcal/mol
N2 = 1.18 ± 0.01
K22 = 2.91 ± 0.54 µM
ΔH2 = 2.90± 0.19 kcal/mol
-TΔS = -10.5 kcal/mol
o
N1 = 0.83 ± 0.05
K21 = 6.39 ± 2.01 nM
ΔH1 = -19.2 ± 0.33 kcal/mol
-TΔS = 7.8 kcal/mol
N2 = 0.90 ± 0.01
K22 = 2.56 ± 0.03 µM
ΔH2 = 2.55 ± 0.26 kcal/mol
-TΔS = -10.4 kcal/mol

Fig8

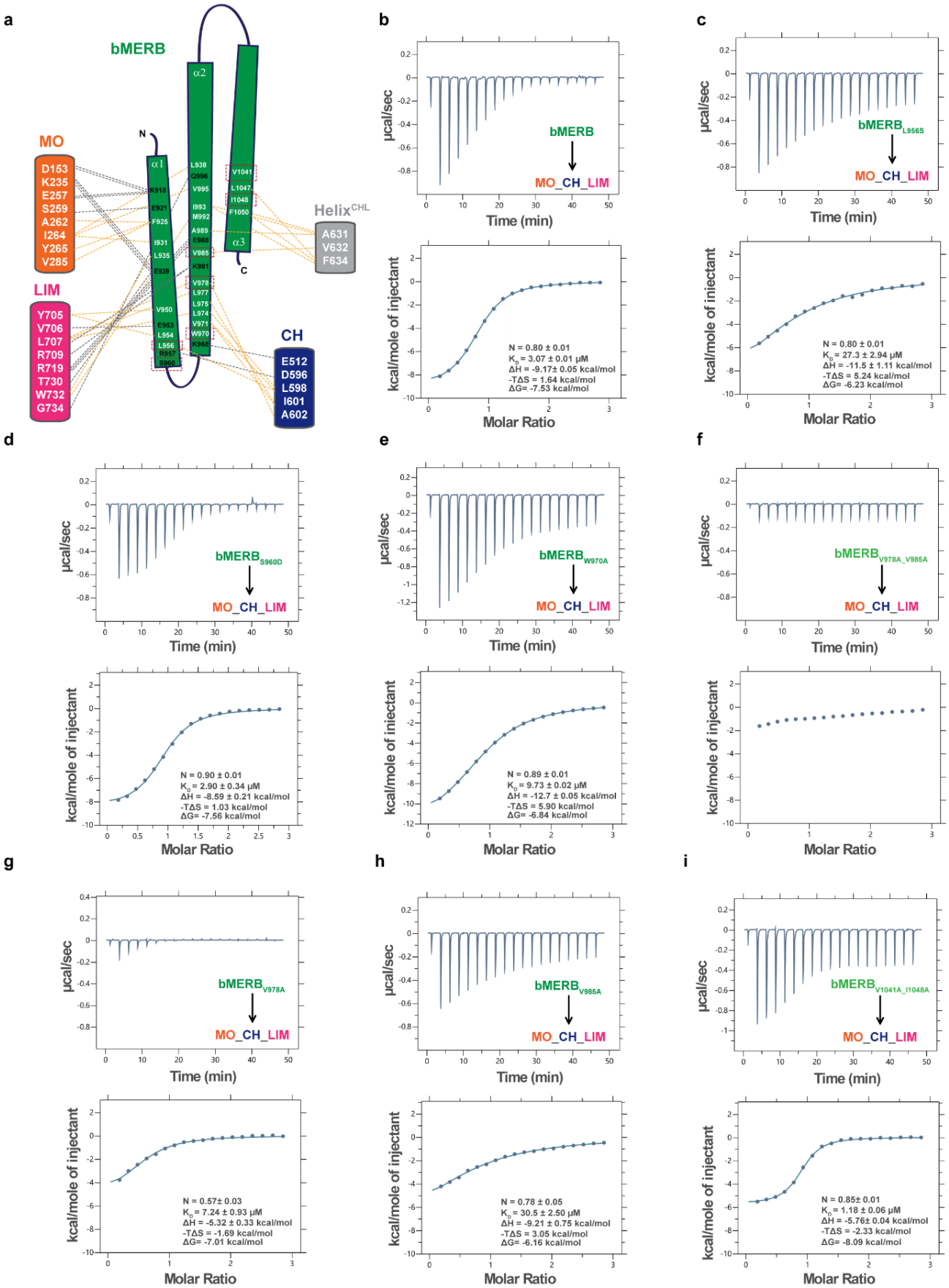
a
bMERB
α2
α1
α3
N
C
MO
D153
K235
E257
S259
A262
I264
Y265
V285
LIM
Y705
V706
L707
R709
R719
T730
W732
G734
HelixCHL
A631
V632
F634
CH
E512
D596
L598
I601
A602
b
bMERB
MO_CH_LIM
Time (min)
μcal/sec
kcal/mole of injectant
Molar Ratio
N = 0.80 ± 0.01
KD = 3.07 ± 0.01 μM
ΔH = -9.17± 0.05 kcal/mol
-TΔS = 1.64 kcal/mol
ΔG= -7.53 kcal/mol
c
bMERBL956S
MO_CH_LIM
N = 0.80 ± 0.01
KD = 27.3 ± 2.94 μM
ΔH = -11.5 ± 1.11 kcal/mol
-TΔS = 5.24 kcal/mol
ΔG= -6.23 kcal/mol
d
bMERBS960D
MO_CH_LIM
N = 0.90 ± 0.01
KD = 2.90 ± 0.34 μM
ΔH = -8.59 ± 0.21 kcal/mol
-TΔS = 1.03 kcal/mol
ΔG= -7.56 kcal/mol
e
bMERBW970A
MO_CH_LIM
N = 0.89 ± 0.01
KD = 9.73 ± 0.02 μM
ΔH = -12.7 ± 0.05 kcal/mol
-TΔS = 5.90 kcal/mol
ΔG= -6.84 kcal/mol
f
bMERBV978A_V985A
MO_CH_LIM
g
bMERBV978A
MO_CH_LIM
N = 0.57± 0.03
KD = 7.24 ± 0.93 μM
ΔH = -5.32 ± 0.33 kcal/mol
-TΔS = -1.69 kcal/mol
ΔG= -7.01 kcal/mol
h
bMERBV985A
MO_CH_LIM
N = 0.78 ± 0.05
KD = 30.5 ± 2.50 μM
ΔH = -9.21 ± 0.75 kcal/mol
-TΔS = 3.05 kcal/mol
ΔG= -6.16 kcal/mol
i
bMERBV1041A_I1048A
MO_CH_LIM
N = 0.85± 0.01
KD = 1.18 ± 0.06 μM
ΔH = -5.76± 0.04 kcal/mol
-TΔS = -2.33 kcal/mol
ΔG= -8.09 kcal/mol

Fig9

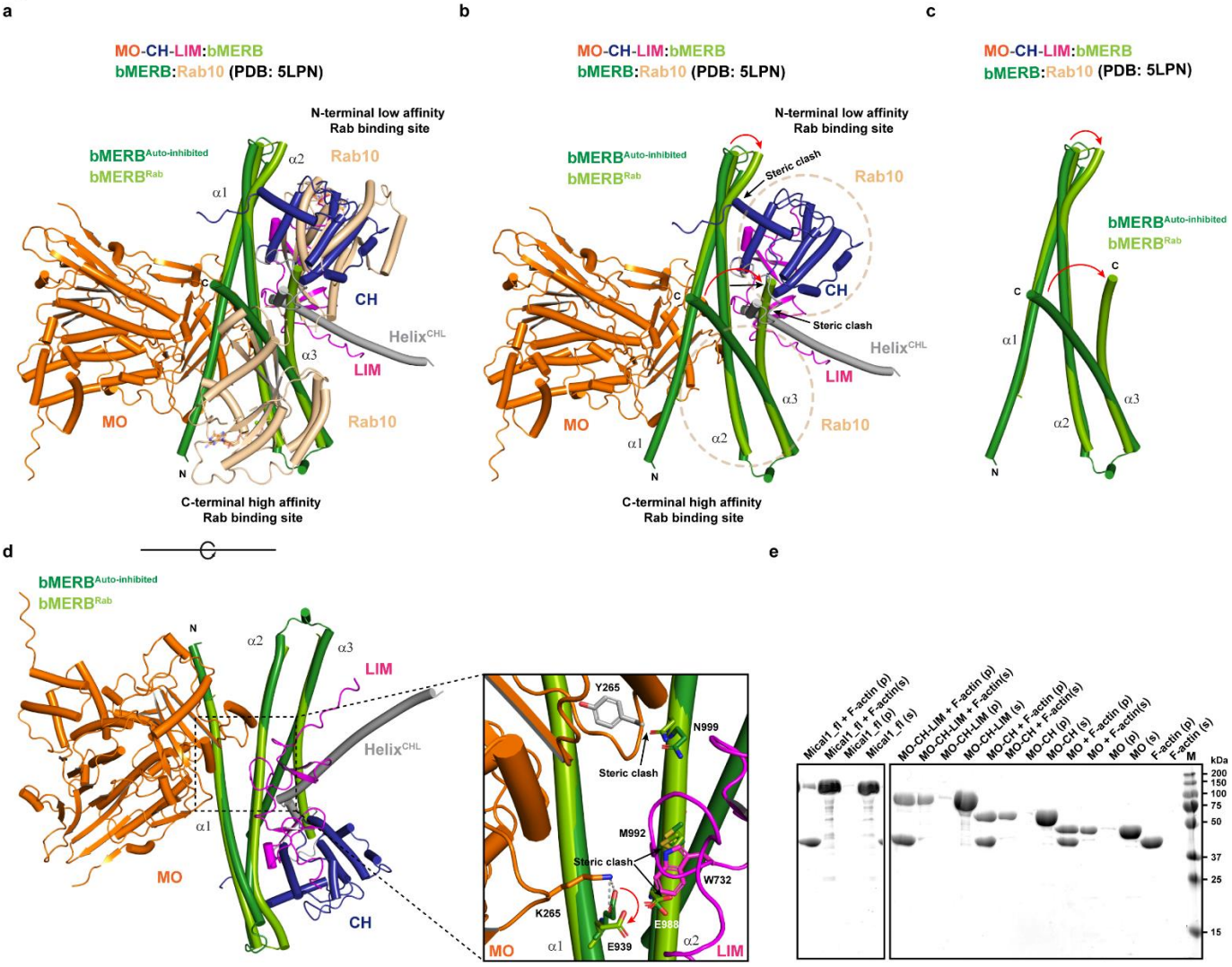
a
MO-CH-LIM:bMERB
bMERB:Rab10 (PDB: 5LPN)
N-terminal low affinity
Rab binding site
bMERBAuto-inhibited
bMERBRab
Rab10
α2
α1
CH
HelixCHL
α3
LIM
MO
Rab10
C-terminal high affinity
Rab binding site
b
MO-CH-LIM:bMERB
bMERB:Rab10 (PDB: 5LPN)
N-terminal low affinity
Rab binding site
bMERBAuto-inhibited
bMERBRab
Steric clash
Rab10
CH
Steric clash
HelixCHL
LIM
α3
MO
α1
α2
Rab10
C-terminal high affinity
Rab binding site
c
MO-CH-LIM:bMERB
bMERB:Rab10 (PDB: 5LPN)
bMERBAuto-inhibited
bMERBRab
α1
α3
α2
d
bMERBAuto-inhibited
bMERBRab
α2
α3
LIM
HelixCHL
α1
MO
CH
Y265
N999
Steric clash
M992
Steric clash
W732
K265
E988
E939
MO
α1
α2
LIM
e
Mical1_fl + F-actin (p)
Mical1_fl + F-actin(s)
Mical1_fl (p)
Mical1_fl (s)
MO-CH-LIM + F-actin (p)
MO-CH-LIM + F-actin(s)
MO-CH-LIM (p)
MO-CH-LIM (s)
MO-CH + F-actin (p)
MO-CH + F-actin(s)
MO-CH (p)
MO-CH (s)
MO + F-actin (p)
MO + F-actin(s)
MO (p)
MO (s)
F-actin (p)
F-actin (s)
M
kDa
200
150
100
75
50
37
25
15

Fig10

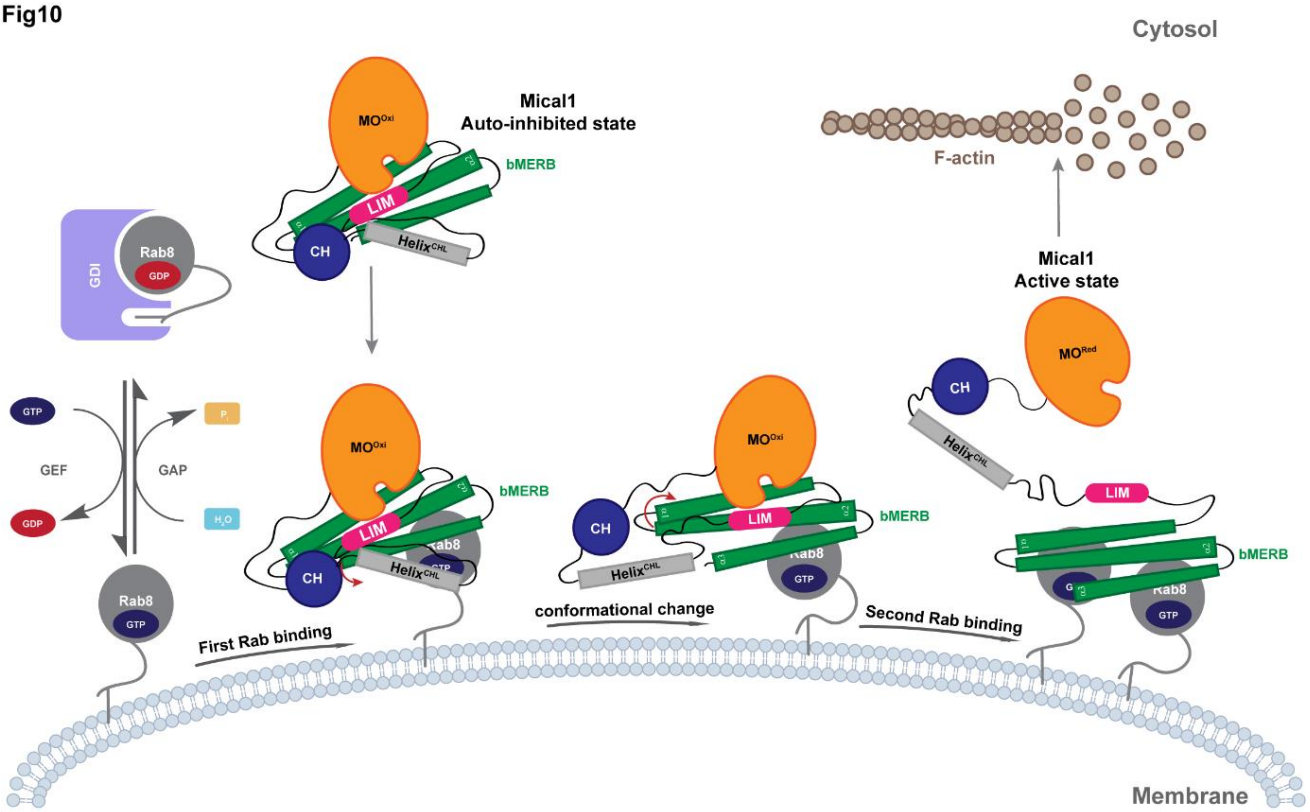
Cytosol
Mical1
Auto-inhibited state
MO^Oxi
bMERB
LIM
CH
Helix^CHL
F-actin
Mical1
Active state
MO^Red
GDI
Rab8
GDP
GTP
GEF
GAP
P_i
H_2O
First Rab binding
conformational change
Second Rab binding
Membrane